A Study of a Quantum Energy-Transport Model for Semiconductors

Submitted to
Graduate School of Information Science and Technology
Osaka University
January 2014

Shohiro SHO

Journal Articles

1. Shohiro Sho and Shinji Odanaka, A quantum energy transport model for semiconductor device simulation, Journal of Computational Physics, 235 (2013), 486-496.

International Conference Presentations

1. Shohiro Sho, Shinji Odanaka, and Akira Hiroki, Analysis of carrier transport in Si and Ge MOSFETs including quantum confinement and hot carrier effects, Proceeding of International Workshop on Computational Electronics, pp. 160-161, June, 2013.

2. Shohiro Sho, Shinji Odanaka, Numerical methods for a quantum energy transport model arising in scaled MOSFETs, Proceedings of International Conference on Simulation of Semiconductor Processes and Devices(SISPAD), pp. 303-306, September, 2011.

Domestic Conference Presentations

1. Shohiro Sho and Shinji Odanaka, Advanced MOSFET simulations using a quantum energy transport model, 電子情報通信学会 シリコン材料・デバイス研究会 (SDM), pp. 32-37, 2013 年 11 月.

2. Shohiro Sho and Shinji Odanaka, A quantum hydrodynamic model for the carrier transport simulation of scaled MOSFETs, 第 60 回応用物理学会春季学術講演会 半導体モデリング・シミュレーションの現状と将来展望, p. 10, 2013 年 3 月.

3. Shohiro Sho and Shinji Odanaka, Numerical scheme and iterative solution method for a quantum energy transport model arising in semiconductor, 日本応用数理学会 2012 年度年会, pp. 357-358, 2012 年 8 月.

4. Shohiro Sho and Shinji Odanaka, Numerical simulation for a quantum energy transport model arising in semiconductor, 日本応用数理学会 2012 年度年会, 2012 年 8 月.

Preface

The performance of semiconductor devices primarily relies on carrier transport properties in the short channels. New device structures (e.g. high-k/metal gate MOSFETs and FinFETs) and new channel materials (e.g. Ge and Ⅲ-Ⅴ compound semiconductors) are needed to achieve high performance and low power CMOS devices (refer to [1]). For this reason, the numerical simulation of quantum hydrodynamics in semiconductors is a major concern to understand the quantum effects and hot carrier effects in scaled devices. The quantum hydrodynamic(QHD) model is derived from a moment expansion of the Wigner-Boltzmann equation adding a collision term by Gardner in [2]. The quantum energy transport(QET) and quantum drift diffusion(QDD) models are further derived by a diffusion approximation of the QHD models. These models consist of a hierarchy of the quantum hydrodynamic models (refer to [3]).

This thesis addresses a quantum energy transport model for carrier transport simulations in scaled semiconductor devices. In classical models, Bløtekjær [4] derived a hydrodynamic(HD) model by taking three moments of Boltzmann transport equation(BTE) with the Fourier law closure. As shown in [5, 6], the energy transport(ET) model is a parabolic-elliptic system, which is derived by a diffusion approximation of the HD model. For classical hydrodynamic simulations, the difficulties associated with the Fourier law closure has been intensively discussed in [5, 7–9]. To overcome this problem, an ET model based on four moments equations of BTE has been proposed by Lee and Tang [7]. However, the difficulties associated with the Fourier law closure remain in QET models. In previous works, the QET models are derived from three moments equations of Wigner-Boltzmann equation with the Fourier law closure. A full QET model has been derived by Degond [10] from the collisional Wigner-Boltzmann equations using the entropy minimization principle. Numerical simulations using this model, however, have not been performed (refer to [11]). Simplified QET models have been proposed as the energy transport extension of the QDD model and numerically

investigated by Jin et al. [12] and Chen and Liu [13]. In [13], the carrier temperature in the current density is further approximated by the lattice temperature to bring the QET model into a self-adjoint form. A four moments QET model has been newly developed by Sho and Odanaka [14]. Numerical methods for the stationary four moments QET system are further presented in [14]. The numerical stability is achieved by developing high accurate schemes and an iterative solution method in terms of a new set of variables. In analogy to the classical ET models (refer to [15, 16]), an extension of Scharfetter-Gummel schemes is developed. For the numerical stability of the solution method, Sho and Odanaka [14] further develop an iterative solution method by introducing an under relaxation method.

This thesis is organized as follows. Chapter 1 discusses the Wigner-Boltzmann equation for the modeling of semiconductor transport. The QHD, QET, and QDD models are introduced as a hierarchy of carrier transport models in semiconductors. In Chapter 2, we derive a 4 moments QET model from four-moments equations derived from the collisional Wigner-Boltzmann equation. Chapter 3 presents the space discretization of the 4 moments QET model. The discretization of the QET system is performed by a new set of unknown variables. We can rewrite the current continuity equation and energy balance equation in the same self-adjoint form, considering the conservation of the current density and the total energy flow. This approach allows us to construct the numerical flux of the finite volume method. Chapter 4 addresses an iterative solution method of the 4 moments QET model. The convergence analysis of the numerical method is performed with numerical experiments. In Chapter 5, transport properties in new device structures and new channel materials are evaluated using the 4 moments QET model. A number of authors have focused on numerical and theoretical studies of carrier transport in MOSFETs on high mobility substrates and Silicon (refer to [17–23]). The numerical results using the QET model are obtained for bulk and double gate Silicon, Germanium, $In_{0.53}Ga_{0.47}As$ n-MOSFET with high-k/metal gate (refer to [24, 25]). Chapter 6 summarizes and concludes this thesis.

Acknowlagements

First of all, I would like to express my sincere gratitude to Professor Shinji Odanaka of Osaka University. I could not have achieved my work without his constant encouragements and valuable comments.

I want to express my appreciation to my thesis advisors, Professor Akitaka Matsumura, Associate Professors Tsuyoshi Chawanya and Daisuke Furihata of Osaka University for his expert guidance and constant support throughout the course of this work.

Thanks are due to Professor Yiming Li of National Chiao Tung University and Associate Professor Akira Hiroki of Kyoto Institute of Technology for valuable discussions and their incisive comments.

I also wish to thank the members in the Cybermedia Center Computer Assisted Science Division of Osaka University.

Last, but certainly not least I want to thank my family, without whom I would never have been able to achieve so much.

Contents

List of Figures

Chapter 1

A hierarchy of transport models

In scaled semiconductor devices, the carrier transport properties primarily depend on the quantum effects and hot carrier effects. For the modeling of such carrier transport in semiconductors, the quantum hydrodynamic(QHD) models have been derived from a Chapman-Enskog expansion of the Wigner-Boltzmann equation adding a collision term (cf. [2,26]). Using a diffusion approximation, the quantum energy transport(QET) and quantum drift diffusion(QDD) models are further derived. In Chapter 1, we discuss the Wigner-Boltzmann equation for the modeling of semiconductor transport. The QHD, QET, and QDD models are introduced as a hierarchy of carrier transport models in semiconductors.

1.1 Wigner-Boltzmann equation

The Wigner-Boltzmann equation is derived from the Wigner-Wyle transformation of Schrödinger equation. We start with a single-state Schrödinger equation on $\mathbf{R}^d$, d=1,2, or 3,

$$i\hbar\frac{\partial}{\partial_t}\psi_i(x,t) = -\frac{\hbar^2}{2m}\nabla^2\psi_i(x,t) + V(x,t)\psi_i(x,t), \tag{1.1.1}$$

where ψ_i are wave functions, $V(x,t)$ is the potential energy, $\hbar$ and m are the Planck's constant and effective mass. When an ensemble of wave functions ψ_i is given, we define the density matrix ρ by

$$\rho(x,x') = \sum_i \psi_i(x)\psi_i^*(x')\alpha_i, \tag{1.1.2}$$

where ψ^* is the complex conjugate of ψ, and the α_i are the occupation probability for the state i.

If the wave function ψ_i satisfy the Schrödinger equation, the density matrix satisfies the so called Heisenberg equation. The Schrödinger equation for the wave function ψ is written as

$$i\hbar\frac{\partial\psi}{\partial t} = -\frac{\hbar^2}{2m}\nabla_x^2\psi + V\psi. \tag{1.1.3}$$

The complex conjugate of ψ satisfy the following equation:

$$-i\hbar\frac{\partial\psi^*}{\partial t} = -\frac{\hbar^2}{2m}\nabla_x^2\psi^* + V\psi^*. \tag{1.1.4}$$

The straightforward calculation yields that the $\psi\psi^*$ satisfy

$$\begin{aligned} i\hbar\frac{\partial}{\partial t}\psi\psi^* &= i\hbar(\frac{\partial\psi}{\partial t}\psi^* + \psi\frac{\partial\psi^*}{\partial t}) \\ &= (-\frac{\hbar^2}{2m}\nabla_x^2\psi + V(x)\psi)\psi^* - \psi(-\frac{\hbar}{2m}\nabla_{x'}^2\psi^* + V(x')\psi^*) \\ &= (-\frac{\hbar^2}{2m}\nabla_x^2 + V(x))\psi\psi^* - (-\frac{\hbar}{2m}\nabla_{x'}^2 + V(x'))\psi\psi^* \\ &= -\frac{\hbar^2}{2m}(\Delta_x - \Delta_{x'})\psi\psi^* + (V(x) - V(x'))\psi\psi^*. \end{aligned} \tag{1.1.5}$$

Given an ensemble of wave function ψ_i, we obtain the Heisenberg equation for the density matrix from (1.1.2) and (1.1.5):

$$\begin{aligned} i\hbar\frac{\partial\rho}{\partial t} &= i\hbar\sum_i \alpha_i\frac{\partial\psi_i\psi_i^*}{\partial t} \\ &= \sum_i \alpha_i(-\frac{\hbar^2}{2m}(\Delta_x - \Delta_{x'})\psi_i\psi_i^* + (V(x) - V(x'))\psi\psi_i^*) \\ &= -\frac{\hbar^2}{2m}(\Delta_x - \Delta_{x'})\rho(x,x') + (V(x) - V(x'))\rho(x,x'). \end{aligned} \tag{1.1.6}$$

The Winger function is now introduced as the Fourier transform of the rotated density matrix

$$f_w(r,p) = \frac{1}{(2\pi\hbar)^d}\int \rho(r+\frac{1}{2}r', r-\frac{1}{2}r')e^{-\frac{ipr'}{\hbar}}dr', \tag{1.1.7}$$

where p is the molecular momentum. Then the density matrix is written as

$$\rho(r+\frac{1}{2}r', r-\frac{1}{2}r') = \int f_w(r,p')e^{\frac{ip'r'}{\hbar}}dp'. \tag{1.1.8}$$

Carrying out the same transformation in the Heisenberg equation yields an equation similar to the classical Boltzmann equation

$$\frac{\partial}{\partial t} f_w(r,p) + \frac{p}{m}\nabla_r f_w(r,p) - \theta[V] f_w = 0. \tag{1.1.9}$$

The operator θ in the integral representation is given by

$$\theta[V] f_w = \frac{-i}{\hbar}\frac{1}{(2\pi\hbar)^d}\int\int (V(r+\frac{r'}{2}) - V(r-\frac{r'}{2}))f_w(r,p')e^{-\frac{i(p-p')r'}{\hbar}}dp'dr'. \tag{1.1.10}$$

If the potential energy V in (1.1.9) has a Taylor series expansion, the Winger-Boltzmann equation is further written as

$$\frac{\partial}{\partial t} f_w(r,p) + \frac{p}{m}\nabla_r f_w - \nabla_r \cdot \nabla_p f_w - \sum_{\alpha=1}^{\infty}\frac{\hbar^{2\alpha}(-1)^\alpha}{4^\alpha(2\alpha+1)!}(\nabla_r V \cdot \nabla_p f_w)^{2\alpha+1} = 0. \tag{1.1.11}$$

This means that the quantum picture reduces to the classical description in the limit $\hbar \to 0$,

$$\theta[V] f_w \to \nabla_r V \cdot \nabla_p f_w. \tag{1.1.12}$$

The Wigner-Boltzmann equation reduces to the classical collisionless Boltzmann equation. By adding a collision term to (1.1.9), the Wigner-Boltzmann equation is of the form

$$\frac{\partial f_w}{\partial t} + \frac{p}{m}\nabla_r f_w - \theta[V] f_w = Q(f_w), \tag{1.1.13}$$

where $Q(f_w)$ is the collision term.

Fig.1.1 shows a hierarchy of carrier transport models. In analogy to the classical hydrodynamic model, the QHD model is derived form a Chapman-Enskog expansion of the Wigner-Boltzmann equation. QET and QDD models are further derived by using a diffusion approximation of QHD model. The QDD model reduces to the classical drift diffusion(DD) model by the limit $\hbar \to 0$.

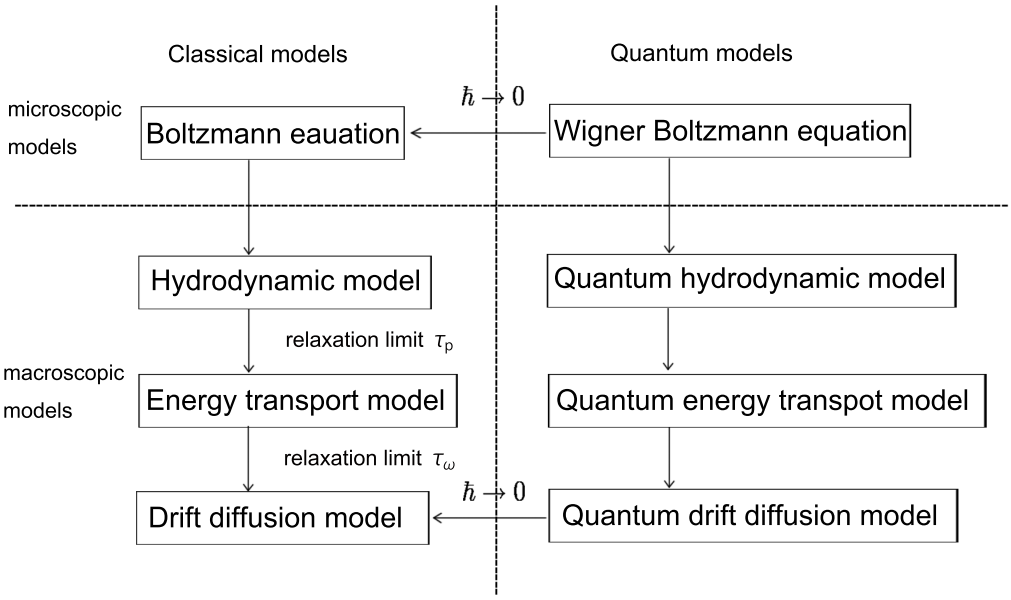

Figure 1.1: A hierarchy of transport models.

1.2 Quantum hydrodynamic model

A QHD model is derived by Gardner [2] from a Chapman-Enskog expansion of the Wigner-Boltzmann equation adding a collision term. Average values of observables A are given in the Wigner formalism by

$$\langle A \rangle = \int A(p) f_w(r,p) dp. \tag{1.2.1}$$

Integrating a function A(p) with respect to p against the Wigner-Boltzmann equation, we obtain

$$\frac{\partial}{\partial t}\langle A \rangle + \nabla_r \langle \frac{p}{m} \cdot A \rangle + \nabla_r V \langle \nabla_p A \rangle + \sum_{\alpha=1}^{\infty} \frac{\hbar^{2\alpha}(-1)^{\alpha+1}}{4^\alpha (2\alpha+1)!} (\nabla_r V \cdot \nabla_p A)^{2\alpha+1} = 0. \tag{1.2.2}$$

Conventionally, the moment expansion of the Wigner-Boltzmann equation involves integrating powers of $A = 1, p, p^2/2m$ against $f_w(x,p)$ in (1.2.2) to obtain conservation laws for particle number, momentum, and energy as follows:

$$\frac{\partial n}{\partial t} + \frac{1}{m}\frac{\partial \langle p_i \rangle}{\partial x_i} = 0, \tag{1.2.3}$$

$$\frac{\langle p_j\rangle}{\partial t} + \frac{\partial}{\partial x_i}\langle\frac{p_i p_j}{m}\rangle = -n\frac{\partial V}{\partial x_j}, \tag{1.2.4}$$

$$\frac{\partial}{\partial t}\langle\frac{p^2}{2m}\rangle + \frac{\partial}{\partial x_i}\langle\frac{p_i p^2}{2m^2}\rangle = -\frac{1}{m}\langle p_i\rangle\frac{\partial V}{\partial x_i}, \tag{1.2.5}$$

where n is the particle density. We introduce the thermal velocity p'/m, representing the difference between own velocity u and the macroscopic fluid velocity v. Then, the macroscopic fluid velocity v is related to the molecular momentum p and a random part p' by

$$p = mv + p'. \tag{1.2.6}$$

The momentum density Π_j, the stress tensor P_{ij}, and the energy density W are defined as follow:

$$\Pi_j = \langle p_j\rangle, \tag{1.2.7}$$

$$P_{ij} = -\langle\frac{p'_i p'_j}{m}\rangle, \tag{1.2.8}$$

$$W = \langle\frac{p^2}{2m}\rangle. \tag{1.2.9}$$

Using the Wigner distribution function and expanding p according to (1.2.6), we have

$$\Pi_j = mnv_j, \tag{1.2.10}$$

$$\langle\frac{p_i p_j}{m}\rangle = \langle\frac{(mv_i + p'_i)(mv_j + p'_j)}{m}\rangle = mv_i v_j\langle 1\rangle + \langle\frac{p'_i p'_j}{m}\rangle = v_i\Pi_j - P_{ij}, \tag{1.2.11}$$

$$W = \langle\frac{p_i p_j}{m}\rangle = \langle\frac{(mv_i + p'_i)(mv_j + p'_j)}{2m}\rangle = \frac{1}{2}mnv^2 + \langle\frac{p'^2}{2m}\rangle \tag{1.2.12}$$

$$\langle\frac{p'_i p_j^2}{2m}\rangle = \langle\frac{p'_i(mv + p')(mv + p')}{2m^2}\rangle = \langle\frac{p'_i p'^2}{2m^2}\rangle + \frac{v_j^2}{2}\langle p'_i\rangle + \frac{v_j}{m}\langle p'_i p'_j\rangle = q_i - v_j P_{ij}, \tag{1.2.13}$$

where the heat flux term q is defined as

$$q_i = \langle\frac{p'_i p'^2}{2m^2}\rangle. \tag{1.2.14}$$

From (1.2.12) and (1.2.13), we obtain

$$\langle\frac{p_i p^2}{2m}\rangle = \langle\frac{(mv_i + p'_i)p^2}{2m^2}\rangle = \langle\frac{p'_i p^2}{2m^2}\rangle + v_i\langle\frac{p^2}{2m}\rangle = v_i W - v_j P_{ij} + q_i. \tag{1.2.15}$$

In previous works (cf. [2, 26]), the heat flux term q is further approximated by the Fourier law

$$q_i = -\kappa(T)\nabla T, \tag{1.2.16}$$

where the thermal conductivity $\kappa(T)$, based on the Wiedemann-Franz law, is given as

$$\kappa(T) = (\frac{5}{2} - c)(\frac{k}{q})^2 q\mu nT, \tag{1.2.17}$$

where c is a fitting parameter. μ and T are the carrier mobility and temperature, respectively. Substituting the expressions (1.2.7), (1.2.11), (1.2.12), and (1.2.13) into the moment equations (1.2.3)-(1.2.5) respectively, we obtain the QHD model without the collision term:

$$\frac{\partial n}{\partial t} + \frac{1}{m}\frac{\partial \Pi_i}{\partial x_i} = 0, i = 1, 2, 3., \tag{1.2.18}$$

$$\frac{\partial \Pi_j}{\partial t} + \frac{\partial}{\partial x_i}(v_i \Pi_j - P_{ij}) = -n\frac{\partial V}{\partial x_j}, \tag{1.2.19}$$

$$\frac{\partial W}{\partial t} + \frac{\partial}{\partial x_i}(v_i W - v_j P_{ij} + q_i) = -\frac{\Pi_i}{m}\frac{\partial V}{\partial x_i}. \tag{1.2.20}$$

Similar expression is obtained for holes. (1.2.18), (1.2.19), and (1.2.20) represent conservation of electron number, momentum , and energy, respectively. The quantum correction to the stress tensor P_{ij} was proposed by Ancona and Iafrate [26], and the quantum correction to the energy density $W = nw$ was first derived by Wigner [27], which are given by

$$P_{ij} = -nkT_n\delta_{ij} + \frac{\hbar^2}{12m} n \frac{\partial^2}{\partial x_i \partial x_j} \log n + O(\hbar^4), \tag{1.2.21}$$

$$W = \frac{1}{2}mnv^2 + \frac{3}{2}nkT_n - \frac{\hbar^2}{24m} n \frac{\partial^2}{\partial x_k^2} \log n + O(\hbar^4), \tag{1.2.22}$$

where k is the Boltzmann constant.

Substituting (1.2.21) and (1.2.22) to (1.2.18)-(1.2.20), the QHD model for electrons is derived as a hyperbolic-elliptic system. In one dimension, we obtain the quantum hydrodynamic conservation laws for electron number, momentum, and energy, coupled with the Poisson equation.

$$\frac{\partial n}{\partial t} + \frac{\partial}{\partial x}(nv) = 0, \tag{1.2.23}$$

$$\frac{\partial}{\partial t}(mnv) + \frac{\partial}{\partial x}(mnv^2 + knT_n - \frac{\hbar^2}{12m}n\frac{\partial^2}{\partial x^2}\log n) = -n\frac{\partial V}{\partial x} - \frac{mnv}{\tau_p}, \quad (1.2.24)$$

$$\frac{\partial W}{\partial t} + \frac{\partial}{\partial x}(vn(\frac{5}{2}kT_n + \frac{1}{2}mv^2 - \frac{\hbar^2}{8m}\frac{\partial^2}{\partial x^2}\log n)) - \frac{\partial}{\partial x}(\kappa(T_n)\frac{\partial T_n}{\partial x})$$
$$= -nv\frac{\partial V}{\partial x} - \frac{W - W_0}{\tau_\omega}. \quad (1.2.25)$$

For the collision term, the electron scattering is modeled by the relaxation time approximation with momentum and energy relaxation times τ_p and τ_ω. The QHD model has been introduced as a quantum corrected version of the classical hydrodynamic model with $O(\hbar^2)$ corrections to the stress tensor and energy density.

1.3 Quantum energy transport model

The QET model is a parabolic-elliptic system, which can be derived by a diffusion approximation of the QHD model (refer to [3]). From (1.2.23)-(1.2.25), we get

$$\frac{\partial n}{\partial t} = \frac{\partial}{\partial x}J_n, \quad (1.3.1)$$

$$\tau_p\frac{\partial}{\partial t}J_n - \frac{\tau_p}{q}\frac{\partial}{\partial x}(J_n \otimes \frac{J_n}{n}) - \mu\frac{\partial}{\partial x}(knT_n) + \mu\frac{\partial}{\partial x}(\frac{\hbar^2}{12m}n\frac{\partial^2}{\partial x^2}\log n) = \mu n\frac{\partial V}{\partial x} - J_n, \quad (1.3.2)$$

$$\frac{\partial W}{\partial t} + \frac{\partial}{\partial x}(nS) = \frac{1}{q}J_n\frac{\partial V}{\partial x} - \frac{W - W_0}{\tau_\omega}, \quad (1.3.3)$$

$$nS = -\frac{1}{q}(\frac{5}{2}kT_n + \frac{1}{2}mv^2 - \frac{\hbar^2}{8m}\frac{\partial^2}{\partial x^2}\log n)J_n - \kappa(T_n)\frac{\partial T_n}{\partial x}, \quad (1.3.4)$$

where $J_n = -qnv$ is current density and q is the positive electrostatic charge. The carrier mobility is defined as

$$\mu = \frac{q\tau_p}{m}. \quad (1.3.5)$$

The potential energy is given by

$$V = -q\varphi, \quad (1.3.6)$$

where φ is the electric potential. When the convective term in (1.3.2)

$$\frac{\tau_p}{q}\frac{\partial}{\partial x}(J_n \otimes \frac{J_n}{n}) \quad (1.3.7)$$

is neglected, a parabolic equation system is obtained. Furthermore, it is assumed that the kinetic energy is neglected against the thermal energy, and the time derivatives vanish. We get a stationary 3 moments QET model for electrons coupled with the Poisson equation as follows:

$$\epsilon\Delta\varphi = q(n - p - C), \tag{1.3.8}$$

$$\frac{\partial}{\partial x}J_n = 0, \tag{1.3.9}$$

$$J_n = \mu k\frac{\partial}{\partial x}(nT_n) - q\mu n\frac{\partial\varphi}{\partial x} - \mu\frac{\partial}{\partial x}(\frac{\hbar^2}{12m}n\frac{\partial^2}{\partial x^2}\log n), \tag{1.3.10}$$

$$\frac{\partial}{\partial x}(nS) = -J_n\frac{\partial\varphi}{\partial x} - \frac{3}{2}nk\frac{T_n - T_L}{\tau_\omega}, \tag{1.3.11}$$

$$nS = -\frac{1}{q}(\frac{5}{2}kT_n - \frac{\hbar^2}{8m}\frac{\partial^2}{\partial x^2}\log n)J_n - \kappa(T_n)\frac{\partial T_n}{\partial x}, \tag{1.3.12}$$

where T_L is the lattice temperature. In the 3 moments QET model, the heat flux is approximated by Fourier's law. Similar expression is obtained for holes. As pointed out in [5] and [7], classical 3 moments ET simulations result in the overestimated spreading of carriers. This effect has been related to errors introduced by the closure of the equation system. In fact, the heat flux density is assumed to be proportional to the gradient of a scalar temperature. Fourier law closure cannot include the fact that the heat flux may not be zero even in a homogeneous system. In addition, the Wiedemann-Franz law is actually an approximation for the diffusive component of heat flux. The convective component of heat flux must be included to obtain physical results when the current flow is not negligible. To overcome difficulties associated with the Fourier law, the fourth moment of the Boltzmann transport equation has been taken into account for the classical energy transport(ET) model. A classical 4 moments ET model is proposed by Lee and Tang [7].

1.4 Quantum drift diffusion model

A QDD model, which is also called the density-gradient model in (cf. [26]), is derived from a diffusion approximation to the QHD model. Assuming the electron temperature is equal to the lattice temperature $T_n = T_L$ in the QET model, the QDD model is obtained as follows:

$$\epsilon\Delta\varphi = q(n - p - C), \tag{1.4.1}$$

$$\frac{\partial}{\partial x} J_n = 0, \tag{1.4.2}$$

$$J_n = \mu k T_L \frac{\partial}{\partial x} n - q\mu n \frac{\partial \varphi}{\partial x} - \mu \frac{\partial}{\partial x} (\frac{\hbar^2}{12m} n \frac{\partial^2}{\partial x^2} \log n). \tag{1.4.3}$$

As mentioned in Chapter 2, the quantum correction in (1.4.3) can be rewritten as

$$\frac{\partial}{\partial x} (\frac{\hbar^2}{12m} n \frac{\partial^2}{\partial x^2} \log n) = qn \frac{\partial}{\partial x} \gamma_n, \tag{1.4.4}$$

where the quantum potential is defined as

$$\gamma_n = \frac{\hbar^2}{6mq} \frac{1}{\sqrt{n}} \frac{\partial^2}{\partial x^2} \sqrt{n}. \tag{1.4.5}$$

It is suggested that the fourth-order equation (1.4.3) is split into two second-order equations (cf. [28, 29]) by introducing the generalized chemical potential under Boltzmann statics (cf. [30]),

$$\varphi_n = \varphi - \frac{kT_L}{q} \log(\frac{n}{n_i}) + \gamma_n, \tag{1.4.6}$$

where n_i is the intrinsic carrier density. In this view, the current continuity for electrons is split into the second-order equation in terms of the variable $\rho_n = \sqrt{n}$,

$$2b_n \nabla^2 \rho_n - \gamma_n \rho_n = 0 \tag{1.4.7}$$

and the continuity equation in terms of the generalized chemical potential

$$\frac{\partial}{\partial x} (q\mu n \frac{\partial}{\partial x} \varphi_n) = 0. \tag{1.4.8}$$

(1.4.6) is rewritten as (1.4.7) in terms of ρ_n, which requires the positivity of solution ρ_n from the mathematical point of view. Then, the QDD model can be rewritten as follows:

$$\epsilon \Delta \varphi = q(n - p - C), \tag{1.4.9}$$

$$\frac{\partial}{\partial x} (q\mu n \frac{\partial}{\partial x} \varphi_n) = 0, \tag{1.4.10}$$

$$2b_n \nabla^2 \rho_n - \gamma_n \rho_n = 0. \tag{1.4.11}$$

Chapter 2

4 Moments quantum energy transport model

In analogy to the classical hydrodynamic(HD) models (cf. [5]), the QET models are obtained by using a diffusion approximation in the quantum hydrodynamic(QHD) equations. The QHD model has been derived from the collisional Wigner-Boltzmann equations, assuming the Fourier law closure by Gardner [2]. For classical hydrodynamic simulations, the closure relation based on the four-moments of the Boltzmann equation has been discussed (cf. [7–9]), and the four-moments ET models are developed for simulations of thin body MOSFETs in [5,31]. In Chapter 2, we derive the 4 moments QET model from four moments equations derived from the collisional Wigner-Boltzmann equation.

2.1 Derivation of 4 moments quantum energy transport model

The four moments equations have the same form as the classical hydrodynamic equations (cf. [7]),

$$\partial_t n + \nabla \cdot (n\mathbf{v}) = nC_n, \tag{2.1.1}$$

$$\partial_t (n\mathbf{p}) + \nabla \cdot (nU) - n\mathbf{F}_E = nC_p, \tag{2.1.2}$$

$$\partial_t (nw) + \nabla \cdot (n\mathbf{S}) - n\mathbf{v} \cdot \mathbf{F}_E = nC_\epsilon, \tag{2.1.3}$$

$$\nabla \cdot (nR) - n(wI + U) \cdot \mathbf{F}_E = nC_{p\epsilon}, \tag{2.1.4}$$

where n, $\mathbf{p}$, and w are the electron density, momentum, and kinetic energy, respectively. $\mathbf{v}$, U, $\mathbf{S}$ and R are the velocity, second moment tensor, energy flow, and fourth moment tensor, respectively. I is the identity tensor. $F_E = -qE$, where E is the electric field. C_n, C_p, C_ϵ, and $C_{p\epsilon}$ are the electron generation rate, the production of crystal momentum, the energy production, and the production of the energy flux, respectively. (2.1.1), (2.1.2), (2.1.3), and (2.1.4) represent conservation of particles, momentum, energy, and energy flux, respectively. By assuming parabolic bands, we give the following closure relations for $\mathbf{p}$ and U as

$$\mathbf{p} = m\mathbf{v}, \tag{2.1.5}$$

$$U_{ij} = mv_iv_j - \frac{P_{ij}}{n}, \tag{2.1.6}$$

where m is an effective mass. $i = 1, 2, 3$ and $j = 1, 2, 3$. For the collision terms, we employ a macroscopic relaxation time approximation to drive a QET model as follows:

$$C_n = 0, \tag{2.1.7}$$

$$C_p = -\frac{p}{\tau_p}, \tag{2.1.8}$$

$$C_\epsilon = -\frac{w - w_0}{\tau_\epsilon}, \tag{2.1.9}$$

where τ_p and τ_ϵ are the momentum and energy relaxation times, respectively.

Substituting (2.1.5) and (1.2.21) into (2.1.2), we obtain the moment equations for conservation of electron number and momentum

$$\frac{\partial n}{\partial t} + \frac{\partial}{\partial x_i}(nv_i) = 0, \tag{2.1.10}$$

$$\frac{\partial}{\partial t}(mnv_i) + \frac{\partial}{\partial x_j}(mnv_iv_j + knT_n - \frac{\hbar^2}{12m}n\frac{\partial^2}{\partial x_i\partial x_j}\log n) = -n\frac{\partial V}{\partial x_i} - \frac{mnv_i}{\tau_p}. \tag{2.1.11}$$

We further get the following relation:

$$\frac{\partial}{\partial x_i}n\frac{\partial^2}{\partial x_i\partial x_j}\log n = 2n\frac{\partial}{\partial x_j}\frac{1}{\sqrt{n}}\frac{\partial^2}{\partial x_i^2}\sqrt{n}. \tag{2.1.12}$$

In fact, the left side of (2.1.12) reads

$$\begin{aligned}\frac{\partial}{\partial x_i}n\frac{\partial^2}{\partial x_i\partial x_j}\log(n) &= \frac{\partial}{\partial x_i}(\frac{\partial^2 n}{\partial x_i\partial x_j} - \frac{1}{n}\frac{\partial n}{\partial x_i}\frac{\partial n}{\partial x_j}) \\ &= \frac{\partial^3 n}{\partial x_i\partial x_i\partial x_j} + \frac{1}{n^2}(\frac{\partial n}{\partial x_i})^2\frac{\partial n}{\partial x_j} - \frac{1}{n}\frac{\partial^2 n}{\partial x_i^2}\frac{\partial n}{\partial x_j} - \frac{1}{n}\frac{\partial^2 n}{\partial x_i\partial x_j}\frac{\partial n}{\partial x_i}\end{aligned} \tag{2.1.13}$$

By the direct calculation, the right side of (2.1.12) is written as follows:

$$\begin{aligned} 2n\frac{\partial}{\partial x_j}\frac{1}{\sqrt{n}}\frac{\partial^2}{\partial x_i^2}\sqrt{n} &= 2n\frac{\partial}{\partial x_j}\frac{1}{\sqrt{n}}(\frac{1}{2\sqrt{n}}\frac{\partial^2 n}{\partial x_i^2} - \frac{1}{4n\sqrt{n}}(\frac{\partial n}{\partial x_i})^2) \\ &= 2n\frac{\partial}{\partial x_j}(\frac{1}{2n}\frac{\partial^2 n}{\partial x_i^2} - \frac{1}{4n^2}(\frac{\partial n}{\partial x_i})^2) \\ &= \frac{\partial^3 n}{\partial x_i \partial x_i \partial x_j} + \frac{1}{n^2}(\frac{\partial n}{\partial x_i})^2\frac{\partial n}{\partial x_j} - \frac{1}{n}\frac{\partial^2 n}{\partial x_i^2}\frac{\partial n}{\partial x_j} - \frac{1}{n}\frac{\partial^2 n}{\partial x_i \partial x_j}\frac{\partial n}{\partial x_i} \end{aligned} \tag{2.1.14}$$

From (2.1.13) and (2.1.14), we get the identity (2.1.12). With the relation (2.1.12), the quantum correction term in (2.1.11) is written as

$$-\frac{\hbar^2}{12m}\frac{\partial}{\partial x_i}n\frac{\partial^2}{\partial x_i \partial x_j}\log n = -\frac{\hbar^2 n}{6m}\frac{\partial}{\partial x_i}(\frac{1}{\sqrt{n}}\frac{\partial^2}{\partial x_j^2}\sqrt{n}) = -qn\frac{\partial}{\partial x_i}\gamma_n, \tag{2.1.15}$$

where the term

$$\gamma_n = \frac{\hbar^2}{6mq}\frac{1}{\sqrt{n}}\frac{\partial^2}{\partial x_j^2}\sqrt{n} \tag{2.1.16}$$

is the quantum potential. Then, the conservation of momentum is given by

$$\frac{\partial}{\partial t}(mnv_i) + \frac{\partial}{\partial x_j}(mnv_i v_j + knT_n) - qn\frac{\partial}{\partial x_i}\gamma_n = -n\frac{\partial V}{\partial x_i} - \frac{mnv_i}{\tau_p}. \tag{2.1.17}$$

We can define the current density $J_j = -qnv_j$ and the positive electrostatic charge q. Using a diffusion approximation in (2.1.17), we obtain

$$\tau_p\frac{\partial}{\partial t}J_i - k\mu_n\frac{\partial}{\partial x_i}(nT_n) + qn\mu_n\frac{\partial}{\partial x_i}\gamma_n = \mu_n n\frac{\partial V}{\partial x_i} - J_i, \tag{2.1.18}$$

where $\mu_n = \frac{q\tau_p}{m}$ is the electron mobility. The potential energy is given by

$$V = -q\varphi. \tag{2.1.19}$$

From (2.1.10), (2.1.18) and (2.1.19), we obtain the current continuity equation as follows:

$$\frac{1}{q}divJ_n = 0, \tag{2.1.20}$$

$$J_n = q\mu_n(\nabla(n\frac{kT_n}{q}) - n\nabla(\varphi + \gamma_n)). \tag{2.1.21}$$

In the same way, we obtain the current continuity equation for holes as follows:

$$\frac{1}{q} div J_p = 0, \tag{2.1.22}$$

$$J_p = q\mu_p(\nabla(p\frac{kT_p}{q}) + p\nabla(\varphi - \gamma_p)), \tag{2.1.23}$$

where p , T_p and μ_p are the hole density, hole temperature and hole mobility, respectively. γ_p is the quantum potential which is written as

$$\gamma_n = \frac{\hbar^2}{6mq}\frac{1}{\sqrt{p}}\frac{\partial^2}{\partial x_j^2}\sqrt{p}. \tag{2.1.24}$$

The energy balance equation is derived from (2.1.3) and (2.1.4) (cf. [7]). The collision term in (2.1.2) is rewritten as

$$C_p = -\frac{qv}{\mu_n}. \tag{2.1.25}$$

As in (2.1.25), the collision term in (2.1.4) is modeled as

$$C_{p\epsilon} = -\frac{qS}{\mu_s}, \tag{2.1.26}$$

where μ_s is the energy flow mobility. Neglecting the time derivative term in (2.1.2), we get

$$n\mathbf{F}_E = \nabla \cdot (nU) + n\frac{q\mathbf{v}}{\mu_n}. \tag{2.1.27}$$

Substituting (2.1.27) into (2.1.4), the expression of energy flux S is given as

$$S = \frac{\mu_s}{\mu_n}(wI + U) \cdot \mathbf{v} + \frac{\mu_s}{qn}((wI + U) \cdot \nabla \cdot (nU) - \nabla \cdot (nR)). \tag{2.1.28}$$

Assuming a heated Maxwellian distribution, the fourth moment tensor R is specified by the classical form as

$$R = \frac{5}{2}k^2T_n^2I. \tag{2.1.29}$$

Using closure (2.1.29), an expression for the energy flux density $S_n = nS$ is obtained as

$$S_n = \frac{\mu_s}{\mu_n}(WI + nU) \cdot \mathbf{v} + \frac{\mu_s}{q}((wI + U) \cdot \nabla \cdot (nU) - \nabla \cdot (\frac{5}{2}nk^2T_n^2I)). \tag{2.1.30}$$

The second term of (2.1.30) is the diffusive contributions to the energy flux density which includes the classical form of R. In this work, we develop a QET model, neglecting quantum corrections in the diffusive contributions to the energy flux density. Substituting (2.1.6) and (1.2.22) into (2.1.30), the quantum corrections to the energy density W and stress tensor P_{ij} are included in the drift contributions to the energy flux density S_n and neglected in the diffusive contributions. As a result, we obtain a quantum corrected expression for the energy flux density as

$$S_n = -\frac{\mu_s}{\mu_n}(\frac{5}{2}\frac{kT_n}{q} - \frac{\hbar^2}{24mq}\Delta\log n - \frac{\hbar^2}{12mq}\frac{\partial^2}{\partial x_i \partial x_j}\log n)J_n \\ -\frac{\mu_s}{\mu_n}\frac{5}{2}(\frac{k}{q})^2 q\mu_n n T_n \nabla T_n. \tag{2.1.31}$$

From (2.1.3), we get the energy balance equation as

$$\nabla \cdot S_n = -J_n \cdot \nabla\varphi - \frac{3}{2}kn\frac{T_n - T_L}{\tau_\epsilon}. \tag{2.1.32}$$

Assuming that the velocity v is slowly varying in the device region, the following term in (2.1.32) is approximated as

$$\begin{aligned}\frac{\hbar^2}{12m}\frac{\partial}{\partial x_i}(nv_j\frac{\partial^2}{\partial x_i \partial x_j}\log n) &= \frac{\hbar^2}{12m}v_j\frac{\partial}{\partial x_i}(n\frac{\partial^2}{\partial x_i \partial x_j}\log n) + \frac{\hbar^2}{12m}\frac{\partial v_j}{\partial x_i}(n\frac{\partial^2}{\partial x_i \partial x_j}\log n) \\ &\approx -J_n\frac{\partial}{\partial x_j}\gamma_n. \end{aligned}\tag{2.1.33}$$

In the same way, we obtain the energy balance equation for holes as follows:

$$\nabla \cdot S_p = J_p \cdot \nabla\varphi - \frac{3}{2}kn\frac{T_p - T_L}{\tau_\epsilon}, \tag{2.1.34}$$

$$S_p = \frac{\mu_s}{\mu_p}(\frac{5}{2}\frac{kT_p}{q} - \frac{\hbar^2}{24mq}\Delta\log p - \gamma_p)J_p - \frac{\mu_s}{\mu_p}\frac{5}{2}(\frac{k}{q})^2 q\mu_p p T_p \nabla T_p. \tag{2.1.35}$$

2.2 4 Moments quantum energy transport model

Coupling with the Poisson equation, the 4 moments QET model consists of the following system of equations:

$$\epsilon\Delta\varphi = q(n - p - C), \tag{2.2.1}$$

$$\frac{1}{q}divJ_n = 0, \tag{2.2.2}$$

$$\frac{1}{q}divJ_p = 0, \tag{2.2.3}$$

$$b_n\nabla\cdot(\rho_n\nabla u_n) - \frac{kT_n}{q}\rho_n u_n = -\frac{\rho_n}{2}(\varphi-\varphi_n), \tag{2.2.4}$$

$$b_p\nabla\cdot(\rho_p\nabla u_p) - \frac{kT_p}{q}\rho_p u_p = \frac{\rho_p}{2}(\varphi-\varphi_p), \tag{2.2.5}$$

$$\nabla\cdot S_n = -J_n\cdot\nabla\varphi - \frac{3}{2}kn\frac{T_n-T_L}{\tau_\epsilon}, \tag{2.2.6}$$

$$\nabla\cdot S_p = J_p\cdot\nabla\varphi - \frac{3}{2}kn\frac{T_p-T_L}{\tau_\epsilon}, \tag{2.2.7}$$

$$J_n = q\mu_n(\nabla(n\frac{kT_n}{q}) - n\nabla(\varphi+\gamma_n)), \tag{2.2.8}$$

$$J_p = q\mu_p(\nabla(p\frac{kT_p}{q}) + p\nabla(\varphi-\gamma_p)), \tag{2.2.9}$$

$$S_n = -\frac{\mu_s}{\mu_n}(\frac{5}{2}\frac{kT_n}{q} - \frac{\hbar^2}{24mq}\Delta\log n+\gamma_n)J_n - \frac{\mu_s}{\mu_n}\frac{5}{2}(\frac{k}{q})^2 q\mu_n nT_n\nabla T_n, \tag{2.2.10}$$

$$S_p = \frac{\mu_s}{\mu_p}(\frac{5}{2}\frac{kT_p}{q} - \frac{\hbar^2}{24mq}\Delta\log p-\gamma_p)J_p - \frac{\mu_s}{\mu_p}\frac{5}{2}(\frac{k}{q})^2 q\mu_p pT_p\nabla T_p. \tag{2.2.11}$$

where $v_n = \frac{(\varphi+\gamma_n-\varphi_n)}{2}$, $v_p = \frac{(\varphi_p+\gamma_p-\varphi)}{2}$, $u_n = \frac{q}{kT_n}v_n$ and $u_p = \frac{q}{kT_p}v_p$. φ is the electrostatic potential. φ_n and φ_p are the chemical potential of electrons and holes, respectively. ρ_n and ρ_p are the the root-density of electrons and holes. ϵ, C and T_L are the permittivity of semiconductor, the ionized impurity density and the lattice temperature, respectively. The value of effective mass is given by a single parameter $m_n = 0.26m_0$ in the silicon devices, where m_0 is the mass of a stationary electron. Then, the quantum parameters for electrons and holes become

$$b_n = \frac{\hbar^2}{12qm_n},\ b_p = \frac{\hbar^2}{12qm_p}. \tag{2.2.12}$$

For a temperature dependent mobility model, we apply the simplified Hänsch's mobility model in [32],

$$\frac{\mu(T_n)}{\mu_0} = (1+\frac{3}{2}\frac{\mu_0 k}{q\tau_\epsilon v_s^2}(T_n-T_L))^{-1}, \tag{2.2.13}$$

where μ_0 and v_s are the low-field mobility and saturation velocity, respectively.

From (2.1.16) and (2.2.12), the quantum potential equation is derived as

$$2b_n\nabla^2\rho_n - \gamma_n\rho_n = 0. \tag{2.2.14}$$

In our model, (2.2.14) is replaced by (2.2.4) with respect to the variable u_n by employing an exponential transformation of variable proposed by Odanaka [33]

$$\rho_n = \sqrt{n} = \sqrt{n_i}\exp(\frac{q}{kT_n}v_n). \tag{2.2.15}$$

If the variable u_n is uniformly bounded, the electron density is maintained to be positive. The same expression can be obtained for holes. As mentioned below, this approach provides a numerical advantage for developing the iterative solution method of the QET model as well as the QDD model.

The system (2.2.1)-(2.2.11) are solved in a bounded domain Ω. The boundary $\partial\Omega$ of the domain Ω splits into two disjoint parts Γ_D and Γ_N. The contacts of semiconductor devices are modeled by the boundary conditions on Γ_D, which fulfill charge neutrality and thermal equilibrium. We further assume that no quantum effects occur at the contacts. Here, the boundary conditions are given as follows:

$$\varphi = \varphi_b + \varphi_{appl},\ n = n_D,\ p = p_D,\ u_n = u_D,\ u_p = u'_D,\ T_n = T_p = T_L \text{ on } \Gamma_D, \tag{2.2.16}$$

$$\nabla\varphi\cdot\nu = \nabla J_n\cdot\nu = \nabla J_p\cdot\nu = \nabla u_n\cdot\nu = \nabla u_p\cdot\nu = \nabla S_n\cdot\nu = \nabla S_p\cdot\nu = 0 \text{ on } \Gamma_N, \tag{2.2.17}$$

where φ_b and φ_{appl} are a built-in potential and an applied bias voltage, respectively. ν denotes the unit outward vector along $\partial\Omega$. $u_D = \frac{q}{kT_L}\frac{\varphi_b}{2}$ on the contacts. In MOSFET structures, $u_n = u_0$ at the silicon dioxide interface, where u_0 is a small positive constant.

Chapter 3

Discretization of 4 moments quantum energy transport model

Chapter 3 will discuss space discretization of a 4 moments QET model. The discretization is performed by a new set of unknown variables (φ, u_n, n, p, T_n). For space discretization, the conservation of the current density and the total energy flow is a key issue as discussed in [34,35] for the classical ET models. It is shown in the QET model that the current continuity equation and energy balance equation can be written in the same self-adjoint form. This result allow us to construct the numerical flux of the finite volume method. In order to construct high accuracy nonlinear schemes, an extension of Scharfetter-Gummel type schemes are further developed.

3.1 Current continuity and energy balance equations

For the current density, we have

$$J_n = q\mu_n(\nabla(n\frac{kT_n}{q}) - \frac{q}{kT_n}(n\frac{kT_n}{q})\nabla(\varphi + \gamma_n)). \tag{3.1.1}$$

As pointed out in [34, 35], for discretization of classical ET models, the total energy flow $H = S_n + \varphi J_n$, which consists of both the thermal energy flow S_n and the electrical flow φJ_n, is used to solve the energy balance equation. J_n and S_n can be written in the same form as shown in [31, 36]. In the QET model, the total energy flow can be rewritten as

$$H = S_n + \varphi J_n$$

$$= \widetilde{S}_n + (\varphi + \frac{\mu_s}{\mu_n}(\frac{\hbar^2}{24mq}\Delta \log n + \gamma_n))J_n, \tag{3.1.2}$$

$$\widetilde{S}_n = -\frac{5}{2}\frac{\mu_s}{\mu_n}\frac{kT_n}{q}J_n - \frac{5}{2}\frac{\mu_s}{\mu_n}(\frac{k}{q})^2 q\mu_n n T_n \nabla T_n. \tag{3.1.3}$$

(2.2.6) is replaced by

$$\nabla \cdot \widetilde{S}_n = -J_n \cdot \nabla(\varphi + \frac{\mu_s}{\mu_n}(\gamma_n + \frac{\hbar^2}{24mq}\Delta \log n)) - \frac{3}{2}kn\frac{T_n - T_L}{\tau_\epsilon}. \tag{3.1.4}$$

Substituting (2.2.8) into (3.1.3), for the energy flow, we have

$$\begin{aligned}\widetilde{S}_n &= -\frac{5}{2}\frac{\mu_s}{\mu_n}q\mu_n(\frac{kT_n}{q}\nabla n\frac{kT_n}{q} - \frac{kT_n}{q}n\nabla(\varphi + \gamma_n) + \frac{kT_n}{q}n\nabla\frac{kT_n}{q}) \\ &= -\frac{5}{2}q\mu_s(\nabla n(\frac{kT_n}{q})^2 - \frac{q}{kT_n}n(\frac{kT_n}{q})^2\nabla(\varphi + \gamma_n)).\end{aligned} \tag{3.1.5}$$

When the variable ξ is defined as $\xi = n\frac{kT_n}{q} = n\eta$ in the current density J_n and $\xi = n(\frac{kT_n}{q})^2 = n\eta^2$ in the energy flow $\widetilde{S}_n$, J_n and $\widetilde{S}_n$ can be written in the same form,

$$\nabla \cdot F = \nabla \cdot (C(\nabla\xi - \frac{q}{kT_n}\xi\nabla(\varphi + \gamma_n))), \tag{3.1.6}$$

where F is the flux. The constant C is defined as $C = q\mu_n$ in J_n and $C = -\frac{5}{2}q\mu_s$ in $\widetilde{S}_n$. By projecting (3.1.6) onto a grid line and using the variable $g = \int_{x_i}^{x}\frac{q}{kT_n}\nabla(\varphi + \gamma_n)$, a one-dimensional self-adjoint form is obtained as

$$\frac{d}{dx}F = \frac{d}{dx}(Ce^g\frac{d}{dx}(e^{-g}\xi)). \tag{3.1.7}$$

3.2 Discretization

Space discretization of the four-moments QET model is performed by a new set of unknown variables (φ, u_n, n, p, T_n). For space discretization, the simulation region is divided into computational cells Ω_{ij} centered at (x_i,y_j). The set of locations $x_{i+\frac{1}{2}}$ and $y_{j+\frac{1}{2}}$ are the positions of the interfaces bounding the computational cell. The cell sizes are given by $a_i^x = x_{i+\frac{1}{2}} - x_{i-\frac{1}{2}}$ and $a_j^y = y_{j+\frac{1}{2}} - y_{j-\frac{1}{2}}$, $i = 1 \cdots N_x + 1$ and $j = 1 \cdots N_y + 1$, where N_x and N_y are the numbers of division at horizontal and vertical directions. In a Cartesian grid, each computational cell is rectangular, and variables φ, u_n, n, p, T_n are defined at cell centers and the flux is defined at cell interfaces.

3.2.1 Poisson equation

Because of the strong nonlinearity of the Poisson equation, (2.2.1) is linearized using a Newton method as follows:

$$\epsilon\Delta\varphi^{m+1} - \frac{q^2}{k}(\frac{n^m}{T_n^m} + \frac{p^m}{T_p^m})\varphi^{m+1} = q(n^m - p^m - C) - \frac{q^2}{k}(\frac{n^m}{T_n^m} + \frac{p^m}{T_p^m})\varphi^m, \tag{3.2.1}$$

where m is the iteration number. The electric flux F, which is defined at interfaces bounding the computational cell, is written as

$$F = \epsilon\nabla\varphi. \tag{3.2.2}$$

The Poisson equation is rewritten as

$$\nabla \cdot F - \frac{q^2}{k}(\frac{n}{T_n} + \frac{p}{T_p})\varphi = g(x, y), \tag{3.2.3}$$

where the function $g(x, y)$ is the right-hand side of (3.2.1). Integrating (3.2.3) over the computational cells Ω_{ij} yields

$$\int_{\Omega_{ij}} \nabla \cdot F dS - \int_{\Omega_{ij}} \frac{q^2}{k}(\frac{n}{T_n} + \frac{p}{T_p})\varphi dS. = \int_{\Omega_{ij}} g(x, y)dS \tag{3.2.4}$$

Using Green's theorem, we obtain a discrete form of $\int_{\Omega_{ij}} \nabla \cdot F dS$ as

$$\begin{aligned}\int_{\Omega_{ij}} \nabla \cdot F dS &= \int_{y_{j-\frac{1}{2}}}^{y_{j+\frac{1}{2}}} (F_{i+\frac{1}{2}} - F_{i-\frac{1}{2}})dy + \int_{x_{i-\frac{1}{2}}}^{x_{i+\frac{1}{2}}} (F_{j+\frac{1}{2}} - F_{j-\frac{1}{2}})dx \\ &= a_j^y(F_{i+\frac{1}{2}} - F_{i-\frac{1}{2}}) + a_i^x(F_{j+\frac{1}{2}} - F_{j-\frac{1}{2}}).\end{aligned} \tag{3.2.5}$$

Then, we obtain a discrete form of the Poisson equation:

$$a_j^y(F_{i+\frac{1}{2}} - F_{i-\frac{1}{2}}) + a_i^x(F_{j+\frac{1}{2}} - F_{j-\frac{1}{2}}) - a_i^x a_j^y \frac{q^2}{k}(\frac{n_{ij}}{T_{n_{ij}}} + \frac{p_{ij}}{T_p})\varphi_{ij} = a_i^x a_j^y g_{ij} \tag{3.2.6}$$

In order to find $F_{i+\frac{1}{2}}$, integrating the electric flux F over the interval $[x_i, x_{i+1}]$. Assuming that F is constant in the interval, we get the flux $F_{i+\frac{1}{2}}$ by

$$F_{i+\frac{1}{2}} = \epsilon\frac{\varphi_{i+1,j} - \varphi_{i,j}}{h_{i+1}^x}, \tag{3.2.7}$$

where $h_{i+1}^x = x_{i+1} - x_i$. Similarly, $F_{i-\frac{1}{2}}$, $F_{j+\frac{1}{2}}$ and $F_{j-\frac{1}{2}}$ are obtained as

$$F_{i-\frac{1}{2}} = \epsilon\frac{\varphi_{i,j} - \varphi_{i-1,j}}{h_i^x}, \tag{3.2.8}$$

$$F_{j+\frac{1}{2}} = \epsilon\frac{\varphi_{i,j+1} - \varphi_{i,j}}{h_{j+1}^y}, \tag{3.2.9}$$

$$F_{j-\frac{1}{2}} = \epsilon\frac{\varphi_{i,j} - \varphi_{i,j-1}}{h_j^y}. \tag{3.2.10}$$

Substituting (3.2.7)-(3.2.10) into (3.2.6), the discrete form of the Poisson equation is derived as

$$a_j^y(\epsilon\frac{\varphi_{i+1,j}-\varphi_{i,j}}{h_{i+1}^x}-\epsilon\frac{\varphi_{i,j}-\varphi_{i-1,j}}{h_i^x})+a_i^x(\epsilon\frac{\varphi_{i,j+1}-\varphi_{i,j}}{h_{j+1}^y}-\epsilon\frac{\varphi_{i,j}-\varphi_{i,j-1}}{h_j^y})$$
$$-a_i^x a_j^y\frac{q^2}{k}(\frac{n_{ij}}{T_{n_{ij}}}+\frac{p_{ij}}{T_p})\varphi_{ij}=a_i^x a_j^y g_{ij} \qquad (3.2.11)$$

3.2.2 Quantum potential equations

Space discretization of (2.2.4) is performed following a previous work [33] to achieve a high-accuracy nonlinear scheme. Assuming that the flux is given by $F=\rho_n\nabla u_n$, we integrate (2.2.4) over the computational cells Ω_{ij}. As a result, we have

$$\int_{\Omega_{ij}} b_n\nabla\cdot F dS-\int_{\Omega_{ij}}\frac{kT_n}{q}\rho_n u_n dS \quad=\quad \int_{\Omega_{ij}}-\frac{\rho_n}{2}(\varphi-\varphi_n)dS. \qquad (3.2.12)$$

The flux is defined at interfaces and then we obtain a discrete form as

$$b_n a_j^y(F_{i+\frac{1}{2}}-F_{i-\frac{1}{2}})+b_n a_i^x(F_{j+\frac{1}{2}}-F_{j-\frac{1}{2}})-\frac{kT_{n_{ij}}}{q}u_{n_{ij}}\int_{\Omega_{ij}}\rho_n dS$$
$$=-\frac{1}{2}(\varphi_{ij}-\varphi_{n_{ij}})\int_{\Omega_{ij}}\rho_n dS. \qquad (3.2.13)$$

In order to find $F_{i+\frac{1}{2}}$, integrating the electric flux F over the interval $[x_i, x_{i+1}]$. Assuming that F is constant in the interval, we get the flux $F_{i+\frac{1}{2}}$ by

$$F_{i+\frac{1}{2}}=\frac{u_{n_{i+1,j}}-u_{n_{i,j}}}{\int_{x_i}^{x_{i+1}}\frac{1}{\rho_n}dx}. \qquad (3.2.14)$$

The accuracy of the numerical flux depends on the explicit integration $\int_{x_i}^{x_{i+1}}\frac{1}{\rho_n}dx$ in (3.2.14). In order to construct a higher accuracy nonlinear scheme, an explicit integration $\int_{x_i}^{x_{i+1}}\frac{1}{\rho_n}dx$ is obtained by the piecewise linear approximation of φ and T_n on the interval $[x_i, x_{i+1}]$. Then we have

$$\int_{x_i}^{x_{i+1}} e^{-u_n}dx=\frac{h_{i+1}^x e^{-u_{n_{i+1,j}}}}{B(u_{n_{i+1,j}}-u_{n_{i,j}})}, \qquad (3.2.15)$$

where $B(x)=\frac{x}{e^x-1}$ is the Bernoulli function. Substituting (3.2.15) into (3.2.14) results in the numerical flux introduced by Odanaka in [33]:

$$F_{i+1/2}=\frac{1}{h_{i+1}^x}e^{u_{n_{i+1,j}}}B(u_{n_{i+1,j}}-u_{n_{i,j}})(u_{n_{i+1,j}}-u_{n_{i,j}}). \qquad (3.2.16)$$

Similarly, $F_{i-\frac{1}{2}}$, $F_{j+\frac{1}{2}}$ and $F_{j-\frac{1}{2}}$ are obtained as

$$F_{i-\frac{1}{2}} = \frac{1}{h_i^x} e^{u_{n_{i,j}}} B(u_{n_{i,j}} - u_{n_{i-1,j}})(u_{n_{i,j}} - u_{n_{i-1,j}}), \tag{3.2.17}$$

$$F_{j+\frac{1}{2}} = \frac{1}{h_{j+1}^y} e^{u_{n_{i,j+1}}} B(u_{n_{i,j+1}} - u_{n_{i,j}})(u_{n_{i,j+1}} - u_{n_{i,j}}), \tag{3.2.18}$$

$$F_{j-\frac{1}{2}} = \frac{1}{h_j^y} e^{u_{n_{i,j}}} B(u_{n_{i,j}} - u_{n_{i,j-1}})(u_{n_{i,j}} - u_{n_{i,j-1}}). \tag{3.2.19}$$

At silicon dioxide interface, the explicit integration is obtained by the piecewise constant approximation.

$$\int_{x_i}^{x_{i+1}} e^{-u_n} dx = \frac{a_i^x}{2} \exp(-\frac{(u_{n_{i,j}} + u_0)}{2})). \tag{3.2.20}$$

Then, the nonlinear scheme is derived as

$$F_{i+\frac{1}{2}} = \frac{2}{a_i^x} \exp(\frac{(u_{n_{i,j}} + u_0)}{2}))(u_0 - u_{n_{i,j}}) \tag{3.2.21}$$

An average of ρ_n in each computational cell is obtained by integrating the piecewise linear representation of u_n on the interval $[x_{i-1/2}, x_{i+1/2}]$ and $[y_{j-1/2}, y_{j+1/2}]$. Then we have

$$\int_{x_{i-1/2}}^{x_{i+1/2}} \rho_n dx = (\frac{h_i^x}{2B(\frac{u_{n_{i-1,j}} - u_{n_{i,j}}}{2})} + \frac{h_{i+1}^x}{2B(\frac{u_{n_{i+1,j}} - u_{n_{i,j}}}{2})}) e^{u_{n_{i,j}}}, \tag{3.2.22}$$

$$\int_{x_{j-1/2}}^{x_{j+1/2}} \rho_n dy = (\frac{h_j^y}{2B(\frac{u_{n_{i,j-1}} - u_{n_{i,j}}}{2})} + \frac{h_{j+1}^y}{2B(\frac{u_{n_{i,j+1}} - u_{n_{i,j}}}{2})}) e^{u_{n_{i,j}}}. \tag{3.2.23}$$

After some calculation we have the following approximation:

$$\begin{aligned} \Lambda_{ij} = \int_{\Omega_{ij}} \rho_n dS &= \int_{y_{j-\frac{1}{2}}}^{y_{j+\frac{1}{2}}} \int_{x_{i-\frac{1}{2}}}^{x_{i+\frac{1}{2}}} \rho_n dx dy \\ &= \frac{1}{4} e^{u_{n_{ij}}} \times (\frac{h_i^x h_j^y}{B(\frac{u_{n_{i-1,j}} - u_{n_{i,j}}}{2}) B(\frac{u_{n_{i,j-1}} - u_{n_{i,j}}}{2})} + \frac{h_{i+1}^x h_j^y}{B(\frac{u_{n_{i+1,j}} - u_{n_{i,j}}}{2}) B(\frac{u_{n_{i,j-1}} - u_{n_{i,j}}}{2})} \\ &\quad + \frac{h_i^x h_{j+1}^y}{B(\frac{u_{n_{i-1,j}} - u_{n_{i,j}}}{2}) B(\frac{u_{n_{i,j+1}} - u_{n_{i,j}}}{2})} + \frac{h_{i+1}^x h_j^y}{B(\frac{u_{n_{i+1,j}} - u_{n_{i,j}}}{2}) B(\frac{u_{n_{i,j+1}} - u_{n_{i,j}}}{2})}). \end{aligned} \tag{3.2.24}$$

Substituting (3.2.16)-(3.2.19), (3.2.24) into (3.2.13) leads to a high-accuracy nonlinear scheme developed in [33]

$$\frac{a_j^y}{h_{i+1}^x} b_n e^{u_{n_{i+1,j}}} B(u_{n_{i+1,j}} - u_{n_{i,j}})(u_{n_{i+1,j}} - u_{n_{i,j}}) - \frac{a_j^y}{h_i^x} b_n e^{u_{n_{i,j}}} B(u_{n_{i,j}} - u_{n_{i-1,j}})(u_{n_{i,j}} - u_{n_{i-1,j}})$$

$$+\frac{a_i^x}{h_{j+1}^y} b_n e^{u_{n_{i,j+1}}} B(u_{n_{i,j+1}} - u_{n_{i,j}})(u_{n_{i,j+1}} - u_{n_{i,j}}) - \frac{a_j^y}{h_j^y} b_n e^{u_{n_{i,j}}} B(u_{i,j} - u_{n_{i,j-1}})(u_{n_{i,j}} - u_{n_{i,j-1}})$$

$$-\omega_{ij} u_{n_{ij}} \Lambda_{ij} = -\frac{1}{2}(\varphi_{ij} - \varphi_{n_{ij}})\Lambda_{ij}, \tag{3.2.25}$$

This scheme results in a consistent generalization of the Scharfetter-Gummel expression to the Sturm-Liouville type equation. In the same way, the Scharfetter-Gummel type scheme to the quantum potential equation for holes is obtained.

3.2.3 Current continuity equations

Assuming that the flux is given by $F = Ce^g \nabla(e^{-g}) n\eta$, we integrate (3.1.7) over the computational cells Ω_{ij}. Using Green's theorem, we obtain a discrete form as

$$\int_{\Omega_{ij}} \nabla \cdot F dx = a_j(F_{i+\frac{1}{2}} - F_{i-\frac{1}{2}}) + a_i(F_{j+\frac{1}{2}} - F_{j-\frac{1}{2}}). \tag{3.2.26}$$

In analogy to the quantum potential equation, the approximation of $F_{i+1/2}$ is obtained by integrating the electric flux F over the interval $[x_i, x_{i+1}]$. Then we have

$$F_{i+\frac{1}{2}} = \frac{C(\psi_{i+1,j} - \psi_{i,j})}{\int_{x_i}^{x_{i+1}} e^{-g} dx}, \tag{3.2.27}$$

where $\psi = e^{-g} n\eta$. In order to construct a higher accuracy nonlinear scheme, an explicit integration $\int_{x_i}^{x_{i+1}} e^{-g} dx$ is obtained by the piecewise linear approximation of φ and T_n on the interval $[x_i, x_{i+1}]$ (cf. [15, 16]). Then we have

$$F_{i+\frac{1}{2}} = \frac{C}{\theta_{i+1}^x h_{i+1}^x}(B(\Delta_{i+1}^x) n_{i+1,j} - B(-\Delta_{i+1}^x) n_{i,j}), \tag{3.2.28}$$

where $B(\cdot)$ is the Bernoulli function. The variables θ_{i+1}^x, Δ_{i+1}^x are calculated as follows:

$$\theta_{i+1}^x = \log(\frac{\eta_{i+1,j}}{\eta_{i,j}})/(\eta_{i+1,j} - \eta_{i,j}), \tag{3.2.29}$$

$$\Delta_{i+1}^x = \theta_{i+1}^x((\varphi_{i+1,j} - \varphi_{i,j}) + (\gamma_{n_{i+1,j}} - \gamma_{n_{i,j}}) - (\eta_{i+1,j} - \eta_{i,j})). \tag{3.2.30}$$

Similarly, $F_{i-\frac{1}{2}}$, $F_{j+\frac{1}{2}}$ and $F_{j-\frac{1}{2}}$ are obtained as

$$F_{i-\frac{1}{2}} = \frac{C}{\theta_i^x h_{i+1}^x}(B(\Delta_i^x) n_{i,j} - B(-\Delta_i^x) n_{i-1,j}), \tag{3.2.31}$$

$$F_{j+\frac{1}{2}} = \frac{C}{\theta_{j+1}^y h_{j+1}^y}(B(\Delta_{j+1}^y) n_{i,j+1} - B(-\Delta_{j+1}^y) n_{i,j}), \tag{3.2.32}$$

$$F_{j-\frac{1}{2}} = \frac{C}{\theta_j^y h_j^y}(B(\Delta_j^y) n_{i,j} - B(-\Delta_j^y) n_{i,j-1}). \tag{3.2.33}$$

As a result, the consistent generalization of the Scharfetter-Gummel type scheme to current continuity equation is derived as

$$\frac{a_j^y \mu_n}{\theta_{i+1}^x h_{i+1}^x}(B(\Delta_{i+1}^x)n_{i+1,j} - B(-\Delta_{i+1}^x)n_{i,j}) - \frac{a_j^y \mu_n}{\theta_i^x h_i^x}(B(\Delta_i^x)n_{i,j} - B(-\Delta_i^x)n_{i-1,j})$$
$$+\frac{a_i^x \mu_n}{\theta_{j+1}^y h_{j+1}^y}(B(\Delta_{j+1}^y)n_{i,j+1} - B(-\Delta_{j+1}^y)n_{i,j}) - \frac{a_i^x \mu_n}{\theta_j^y h_j^y}(B(\Delta_j^y)n_{i,j} - B(-\Delta_j^y)n_{i,j-1}) = 0. \tag{3.2.34}$$

In the same way, the Scharfetter-Gummel type scheme to the current continuity equation for holes is obtained.

3.2.4 Energy balance equations

Assuming that the flux is given by $F = Ce^g \nabla(e^{-g})n\eta^2$, we integrate (3.1.4) over the computational cells Ω_{ij}. Using Green's theorem, we obtain a discrete form as

$$a_j^y(F_{i+\frac{1}{2}} - F_{i-\frac{1}{2}}) + a_i^x(F_{j+\frac{1}{2}} - F_{j-\frac{1}{2}}) + a_i^x a_j^y \frac{3}{2} kn \frac{T_n}{\tau_\epsilon}$$
$$= \int_{\Omega_{ij}} -J_n \cdot \nabla(\varphi + \frac{\mu_s}{\mu_n}(\gamma_n + \frac{\hbar^2}{24mq}\Delta \log n))dS + a_i^x a_j^y \frac{3}{2} kn \frac{T_L}{\tau_\epsilon}. \tag{3.2.35}$$

Here, quantum corrections are included in the carrier heating term. Since the energy flow density and the current density can be written in the same form (3.1.7), the numerical flux $F_{i+1/2}$ is derived as

$$F_{i+\frac{1}{2}} = \frac{C}{\theta_{i+1}^x h_{i+1}^x}(B(\Delta_{i+1}^x)n_{i+1,j}\eta_{i+1,j} - B(-\Delta_{i+1}^x)n_{i,j}\eta_{i,j}), \tag{3.2.36}$$

where variables θ_i^x and Δ_i^x are

$$\theta_{i+1}^x = \log(\frac{\eta_{i+1,j}}{\eta_{i,j}})/(\eta_{i+1,j} - \eta_{i,j}), \tag{3.2.37}$$
$$\Delta_{i+1}^x = \theta_{i+1}^x((\varphi_{i+1,j} - \varphi_{i,j}) + (\gamma_{n_{i+1,j}} - \gamma_{n_{i,j}}) - (\eta_{i+1,j} - \eta_{i,j})). \tag{3.2.38}$$

Similarly, $F_{i-\frac{1}{2}}$, $F_{j+\frac{1}{2}}$ and $F_{j-\frac{1}{2}}$ are obtained as

$$F_{i-\frac{1}{2}} = \frac{c_2}{\theta_i^x h_{i+1}^x}(B(\Delta_i^x)n_{i,j}\eta_{i,j} - B(-\Delta_i^x)n_{i-1,j}\eta_{i-1,j}), \tag{3.2.39}$$
$$F_{j+\frac{1}{2}} = \frac{c_2}{\theta_{j+1}^y h_{j+1}^y}(B(\Delta_{j+1}^y)n_{i,j+1}\eta_{i,j+1} - B(-\Delta_{j+1}^y)n_{i,j}\eta_{i,j}), \tag{3.2.40}$$
$$F_{j-\frac{1}{2}} = \frac{c_2}{\theta_j^y h_j^y}(B(\Delta_j^y)n_{i,j}\eta_{i,j} - B(-\Delta_j^y)n_{i,j-1}\eta_{i,j-1}). \tag{3.2.41}$$

To conserve the total energy flow $H = S_n + \varphi J_n$ (3.1.2), discretization of the carrier heating term is another key issue. From Gauss's theorem, the first term on the right hand side of (3.2.35) can be calculated as

$$\begin{aligned}\Lambda_{ij} &= \int_{\Omega_{ij}} -J_n \cdot \nabla(\varphi + \frac{\mu_s}{\mu_n}(\gamma_n + \frac{b_n}{2}\Delta \log n))dx \\ &= -\int_{\partial\Omega_{ij}} (J_n(\varphi + \frac{\mu_s}{\mu_n}(\gamma_n + \frac{b_n}{2}\Delta \log n))) \cdot \nu dx. \end{aligned} \tag{3.2.42}$$

The electron density under the Boltzmann statics is expressed as

$$n = n_i \exp(\frac{q(\varphi + \gamma - \varphi_n)}{kT_n}) = n_i \exp(2u_n), \tag{3.2.43}$$

where n_i is the intrinsic density. Then, the discretization for $\Delta \log n = 2\Delta u_n$ in (3.2.42) is obtained by a standard five-point approximation:

$$\begin{aligned}\Delta^h u_n^h = &\frac{1}{a_j^y h_{j+1}^y} u_{i,j+1} + \frac{1}{a_j^y h_j^y} u_{i,j-1} + \frac{1}{a_i^x h_{i+1}^x} u_{i+1,j} + \frac{1}{a_i^x h_i^x} u_{i-1,j} \\ &-(\frac{h_{j+1}^y + h_j^y}{a_j^y h_{j+1}^y h_j^y} + \frac{h_{i+1}^x + h_i^x}{a_i^x h_{i+1}^x h_i^x}) u_{i,j}. \end{aligned} \tag{3.2.44}$$

The discrete form of the carrier heating term in (3.2.35) yields

$$\begin{aligned}\Lambda_{ij} &= \int_{\Omega_{ij}} -J_n \cdot \nabla(\varphi + \frac{\mu_s}{\mu_n}(\gamma_n + b_n\Delta^h u_n^h))dx \\ &\approx -a_i^x(J_{n_{j+\frac{1}{2}}}(\varphi_{j+\frac{1}{2}} + \frac{\mu_s}{\mu_n}(\gamma_{n_{j+\frac{1}{2}}} + b_n\Delta^h u_n^h)) - J_{n_{j-\frac{1}{2}}}(\varphi_{j-\frac{1}{2}} + \frac{\mu_s}{\mu_n}(\gamma_{n_{j-\frac{1}{2}}} + b_n\Delta^h u_n^h))) \\ &\quad -a_j^y(J_{n_{i+\frac{1}{2}}}(\varphi_{i+\frac{1}{2}} + \frac{\mu_s}{\mu_n}(\gamma_{n_{i+\frac{1}{2}}} + b_n\Delta^h u_n^h)) - J_{n_{i-\frac{1}{2}}}(\varphi_{i-\frac{1}{2}} + \frac{\mu_s}{\mu_n}(\gamma_{n_{i-\frac{1}{2}}} + b_n\Delta^h u_n^h))). \end{aligned} \tag{3.2.45}$$

Then the consistent generalization of the Scharfetter-Gummel type scheme to the energy balance equation is derived as

$$\begin{aligned}&a_j^y(\frac{C}{\theta_{i+1}^x h_{i+1}^x}(B(\Delta_{i+1}^x)n_{i+1,j}\eta_{i+1,j} - B(-\Delta_{i+1}^x)n_{i,j}\eta_{i,j}) - \frac{C}{\theta_i^x h_{i+1}^x}(B(\Delta_i^x)n_{i,j}\eta_{i,j} \\ &-B(-\Delta_i^x)n_{i-1,j}\eta_{i-1,j})) + a_i^x(\frac{C}{\theta_{j+1}^y h_{j+1}^y}(B(\Delta_{j+1}^y)n_{i,j+1}\eta_{i,j+1} - B(-\Delta_{j+1}^y)n_{i,j}\eta_{i,j}) \\ &-\frac{C}{\theta_j^y h_j^y}(B(\Delta_j^y)n_{i,j}\eta_{i,j} - B(-\Delta_j^y)n_{i,j-1}\eta_{i,j-1})) + a_i^x a_j^y \frac{3q}{2\tau_\eta} n_{i,j}\eta_{i,j} = \Lambda_{i,j} + a_i^x a_j^y \frac{3q}{2\tau_\eta} n_{i,j}\eta_0. \end{aligned} \tag{3.2.46}$$

In the same way, the Scharfetter-Gummel type scheme to the energy balance equation for holes is obtained.

Chapter 4

Iterative solution method of 4 moments quantum energy transport model

Chapter 4 will discuss an iterative solution method of 4 moments QET model. The iterative solution method is achieved by a new set of variables. We develop an iterative solution method by introducing an under relaxation method. The convergence behavior of electrostatic potential, quantum potential, electron density, and electron temperature are shown with numerical experiments.

4.1 Iterative solution method

We develop an iterative solution method of the QET model by constructing a Gummel map [37] with a new set of unknown variables (φ, u_n, n, p, T_n) as follows:

(P1) Let φ^m, n^m, p^m, T_n^m are given, solve the nonlinear Poisson equation with respect to the electrostatic potential φ^{m+1}, where m is the number of iteration.

$$\epsilon\Delta\varphi^{m+1} - \frac{q^2}{k}(\frac{n^m}{T_n^m} + \frac{p}{T_p})\varphi^{m+1} = q(n^m - p^m - C) - \frac{q^2}{k}(\frac{n^m}{T_n^m} + \frac{p}{T_p})\varphi^m. \tag{4.1.1}$$

(P2) Let φ^{m+1}, ρ_n^m, φ_n^m, T_n^m are given, solve the potential u_n^{m+1}.

$$b_n\nabla\cdot(\rho_n^m\nabla u_n^{m+1}) - \eta^m\rho_n^m u_n^{m+1} = -\frac{\rho_n^m}{2}(\varphi^{m+1} - \varphi_n^m). \tag{4.1.2}$$

Then, using u_n^{m+1} the quantum potential is further calculated as

$$\gamma_n^{m+1} = 2\eta^m u_n^{m+1} + \varphi_n^m - \varphi^{m+1}. \tag{4.1.3}$$

(P3) Let φ^{m+1}, γ_n^{m+1}, T_n^m are given, solve the electron density n^{m+1}.

$$\frac{1}{q} div J_n = 0, \tag{4.1.4}$$

$$J_n = q\mu_n e^g \nabla(e^{-g} n^{m+1} \eta^m). \tag{4.1.5}$$

We set the generalized chemical potential by

$$\varphi_n^{m+1} = -\eta^m \log \frac{n^{m+1}}{n_i} + \varphi^{m+1} + \gamma_n^{m+1}. \tag{4.1.6}$$

(P4) Let φ^{m+1} is given, solve the hole density p^{m+1}.

$$\frac{1}{q} div J_p = 0, \tag{4.1.7}$$

$$J_p = q\mu_p e^g \nabla(e^{-g} p^{m+1} \frac{kT_p}{q}). \tag{4.1.8}$$

(P5) Let φ^{m+1}, γ_n^{m+1}, n^{m+1}, T_n^m are given, solve the electron temperature T_n^{m+1}.

$$\begin{aligned} &\nabla \cdot \widetilde{S}_n + \frac{3}{2} k \frac{n^{m+1} T_n^{m+1}}{\tau_\epsilon} \\ &= -J_n \cdot \nabla(\varphi^{m+1} + \frac{\mu_s}{\mu_n}(\gamma_n^{m+1} + b_n \Delta u_n^{m+1})) + \frac{3}{2} k \frac{n^{m+1} T_L}{\tau_\epsilon}. \end{aligned} \tag{4.1.9}$$

An iterative solution method, which consists of the inner and outer iteration loops, is developed, as shown in Fig.4.1. The algorithm using the variable u_n in (2.2.4) ensures the positivity of the root-density of electrons without introducing damping parameters (cf. [33]). In fact, it is a critical issue to solve for the root-density ρ_n the quantum potential equation

$$-2b_n \nabla^2 \rho_n + \gamma_n \rho_n = 0. \tag{4.1.10}$$

In this case, the iterative solution method requires an additional iteration loop to maintain positive solutions for the root- density of electrons in the inner iteration loop as pointed out by de Falco et al. [38, 39]. Hence, in the inner iteration loop, (4.1.10) is replaced by (2.2.4) to ensure the positivity of the root density of electrons. Moreover,

we can enhance the robustness of the iterative solution method by introducing an under relaxation method with a parameter α, $0 < \alpha < 1$, in the outer iteration loop:

$$T^{m+1} = T^m + \alpha(T_*^{m+1} - T^m). \tag{4.1.11}$$

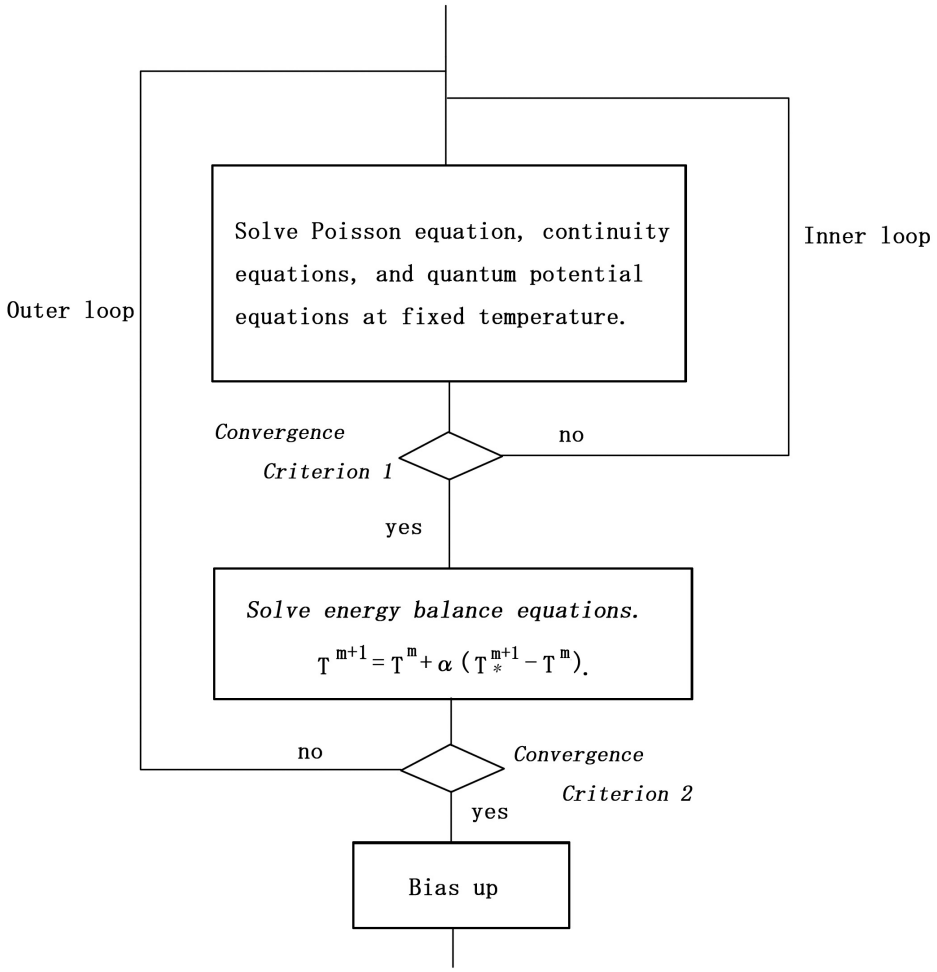

Figure 4.1: An iterative solution method with a relaxation algorithm.

4.2 Numerical experiments

We can construct a numerical method for the QET model in terms of the variables (φ, u_n, n, p, T_n), using the space discretization and the iterative solution method mentioned

above. The convergence analysis of the numerical method is performed with numerical experiment on a two dimensional Bulk n-MOSFET. The outer error estimates are plotted in Figs.4.2, 4.3, 4.4, and 4.5. The relative error for electron temperature and electron density are estimated as

$$\|T\| = \max_{i,j} \frac{|T^m_{n_{ij}} - T^{m-1}_{n_{ij}}|}{|T^m_{n_{ij}}|}, \tag{4.2.1}$$

$$\|n\| = \max_{i,j} \frac{|n^m_{ij} - n^{m-1}_{ij}|}{|n^m_{ij}|}. \tag{4.2.2}$$

For the electrostatic potential and quantum potential, the norm is defined by the maximum differences between outer iterations:

$$\|\varphi\| = \max_{i,j} |\varphi^m_{ij} - \varphi^{m-1}_{ij}|, \tag{4.2.3}$$

$$\|u\| = \max_{i,j} |u^m_{ij} - u^{m-1}_{ij}|. \tag{4.2.4}$$

Figs.4.2 and 4.3 show the relative error of electron temperature and electron density vs. number of Gummel iterations, respectively. The error estimates of electrostatic potential and quantum potential are shown in Figs.4.4 and 4.5. The error estimates are calculated at the bias condition $V_g = 0.8V$ and $V_d = 0.0 \rightarrow 0.2$. It is found that the error rapidly decreases as the number of Gummel iterations increases. In Fig.4.2, the convergence behavior of electron temperature between three different relaxation parameters $\alpha = 0.2, 0.5, 0.8$ are compared. It is clear that the numerical stability is obtained by the relaxation method.

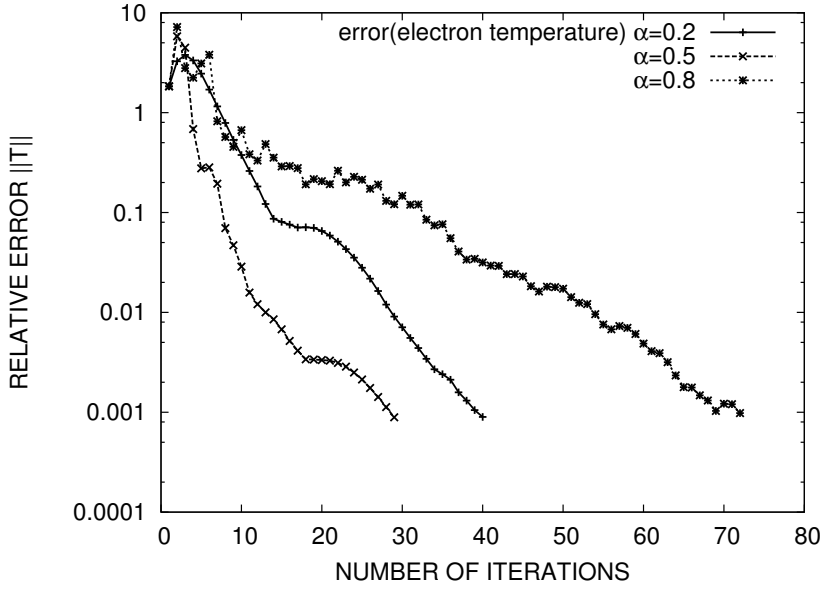

Figure 4.2: Relative error of electron temperature vs. number of Gummel iterations at different relaxation parameters.

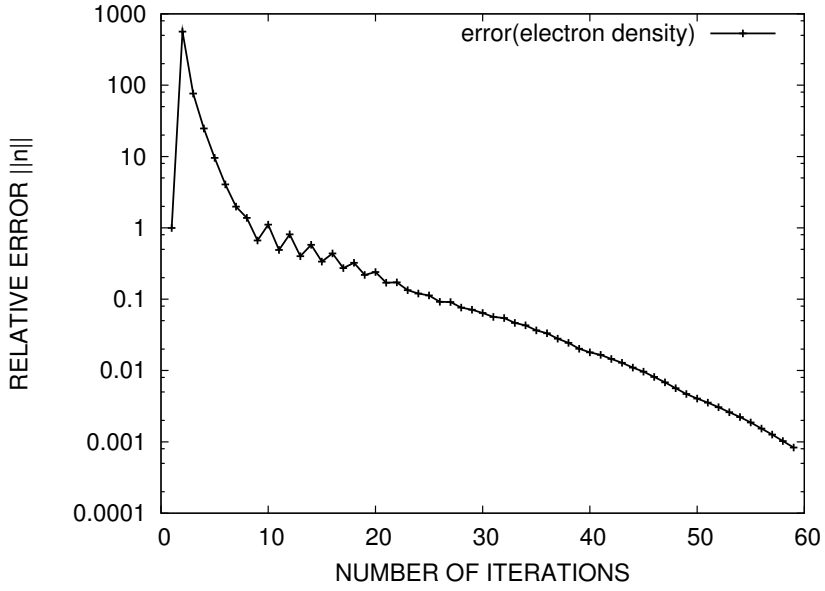

Figure 4.3: Relative error of electron density vs. number of Gummel iterations.

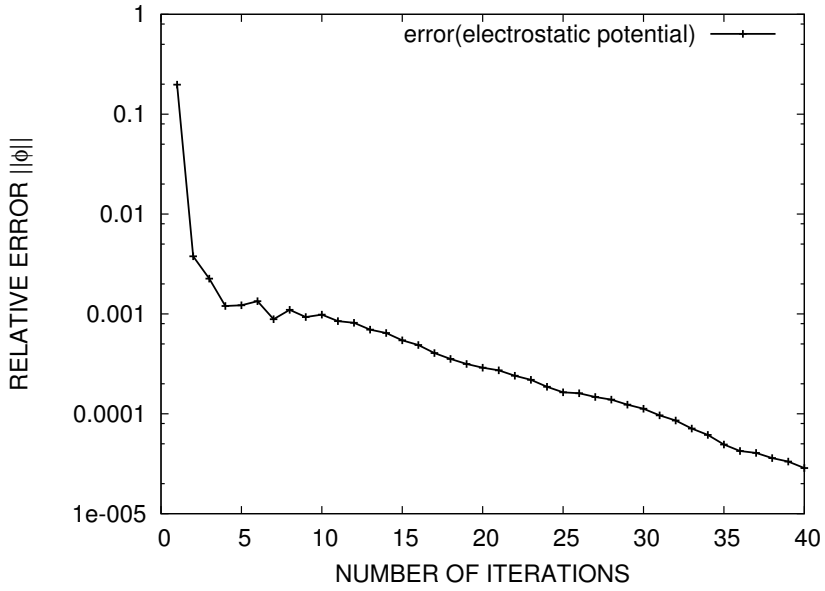

Figure 4.4: Error of electrostatic potential vs. number of Gummel iterations.

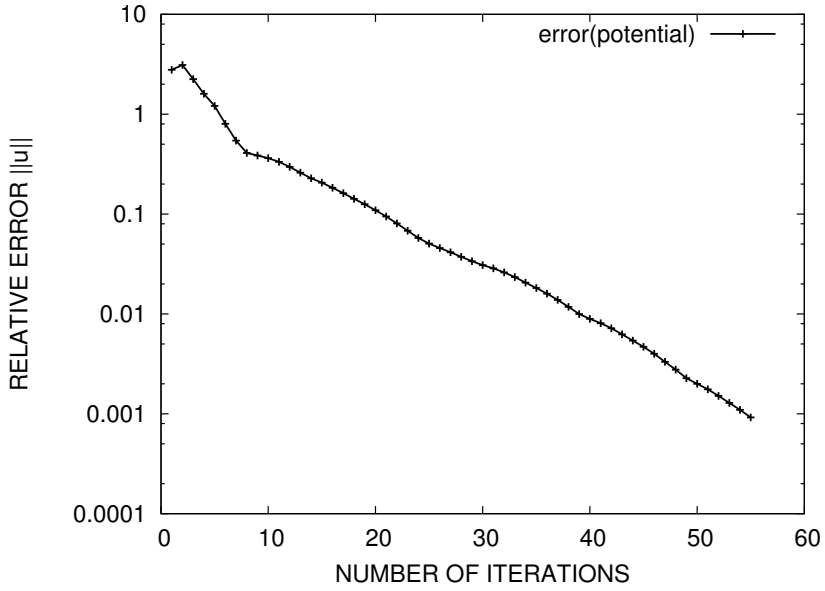

Figure 4.5: Error of quantum potential vs. number of Gummel iterations.

Chapter 5

Simulation results for MOSFET structures

New channel materials such as Ge and III-V semiconductors are needed to achieve high performance and low power CMOS devices (cf. [17]). In Chapter 5, transport properties in Si, Ge and $In_{0.53}Ga_{0.47}As$ n-MOSFETs are evaluated using a 4 moments QET model. The simulation results for bulk and double gate Si, Ge, $In_{0.53}Ga_{0.47}As$ n-MOSFETs with high-k/metal gate are examined. The QET model reveals carrier transport properties including quantum confinement and hot carrier effects.

5.1 Simulation condition

The transport properties of Si, Ge, and $In_{0.53}Ga_{0.47}As$ are obtained for 35nm n-MOSFETs. Selected material parameters are listed in Table 5.1. The saturation velocities are selected an average value in the inversion layer. Figs. 5.1 and 5.2 show two-dimensional cross sections of 35nm bulk and double gate MOSFETs, respectively. Both devices have effective oxide thickness(EOT)=0.7nm and the S/D doping of 4.0×10^{19} cm^{-3}. The channel doping is 1.0×10^{18} in the bulk n-MOSFET and 1.0×10^{17} in the double gate n-MOSFET. The dielectric permittivity considered here is 22, and the value is known as "HfO_2". For metal gates, the work functions of 4.36 eV for Si, 4.14 eV for Ge, and 4.51 eV for $In_{0.53}Ga_{0.47}As$ devices are adopted. The energy relaxation time τ_ϵ of 0.1×10^{-12} s and a ratio μ_s/μ_n of 0.8 are chosen. For the n-MOSFETs simulation, we assume hole temperature T_p=T_L.

The QET model includes a two-dimensional calculation of the electrostatic poten-

tial in the region with boundary A-G-L-F, and a two-dimensional calculation of the variables u_n, u_p, n, p, and T_n in the silicon region with boundary A-B-E-F. The mixed boundary conditions for the QET system are assigned as follows:
For the electrostatic potential φ and chemical potentials φ_n and φ_p

$$\varphi = \varphi_{appl} + \varphi_b, \tag{5.1.1}$$

$$\varphi_n = \varphi_p = \varphi_{appl}, \tag{5.1.2}$$

at source and drain regions, and back gate, where φ_{appl} is the applied bias voltage, and φ_b is the built-in potential, respectively. The gate region is also treated as a Dirichlet boundary condition with an approximated work function of the material. At the sides A-B, H-I, J-K, E-F, we have the homogeneous Neumann condition

$$\frac{\partial \varphi}{\partial \nu} = \frac{\partial \varphi_n}{\partial \nu} = \frac{\partial \varphi_p}{\partial \nu} = 0. \tag{5.1.3}$$

For the variables u_n, n, p, and T_n, we have the following Dirichlet conditions:

$$\begin{aligned}
u_n &= \begin{cases} (q\varphi_b)/(2kT_n) \text{ at sides B} - \text{C, D} - \text{E, and A} - \text{F,} \\ u_0 \text{ at the silicon} - \text{oxide interface C} - \text{D,} \end{cases} \\
u_p &= \begin{cases} -(q\varphi_b)/(2kT_p) \text{ at sides B} - \text{C, D} - \text{E, and A} - \text{F,} \\ u_0 \text{ at the silicon} - \text{oxide interface C} - \text{D,} \end{cases} \\
n &= \begin{cases} (C + \sqrt{C^2 + 4n_i^2})/2 \text{ at sides B} - \text{C and D} - \text{E,} \\ n_i^2/p \text{ at the back gate,} \end{cases} \\
p &= \begin{cases} n_i^2/n \text{ at sides B} - \text{C and D} - \text{E,} \\ (-C + \sqrt{C^2 + 4n_i^2})/2 \text{ at the back gate,} \end{cases} \\
T_n &= T_L \text{ at sides B} - \text{C, D} - \text{E, and A} - \text{F,}
\end{aligned} \tag{5.1.4}$$

where u_0 is the small positive constant. The carrier densities are assumed to fulfill charge neutrality and thermal equilibrium at the contacts. We further assume that no quantum effects occur at the contacts. At the sides A-B and E-F, the homogeneous Neumann conditions read:

$$\frac{\partial u_n}{\partial \nu} = \frac{\partial u_p}{\partial \nu} = \frac{\partial n}{\partial \nu} = \frac{\partial p}{\partial \nu} = \frac{\partial T_n}{\partial \nu} = 0, \tag{5.1.5}$$

at the side C-D,

$$\frac{\partial n}{\partial \nu} = \frac{\partial p}{\partial \nu} = \frac{\partial T_n}{\partial \nu} = 0. \tag{5.1.6}$$

The mixed boundary conditions are similarly assigned to the double gate n-MOSFET.

Table 5.1: Selected Semiconductor Material Parameters

semiconductor	Si	Ge	$In_{0.53}Ga_{0.47}As$
$\mu_{eff}(cm^2/Vs)$	400 [19]	1040 [19]	4000 [22]
$E_G(eV)$	1.12 [20]	0.66 [20]	0.73 [20]
$\epsilon_R(\epsilon_0)$	11.7 [20]	16.0 [20]	14.0 [20]
$m_{eff}(m_0)$	0.26 [42]	0.12 [42]	0.048 [20]
$n_i(cm^{-3})$	1.08×10^{10} [42]	1.64×10^{13} [42]	9.0×10^{11} [23]
$v_{sat}(cm/s)$	1.0×10^7 [21]	0.7×10^7 [21]	0.75×10^7 [21]

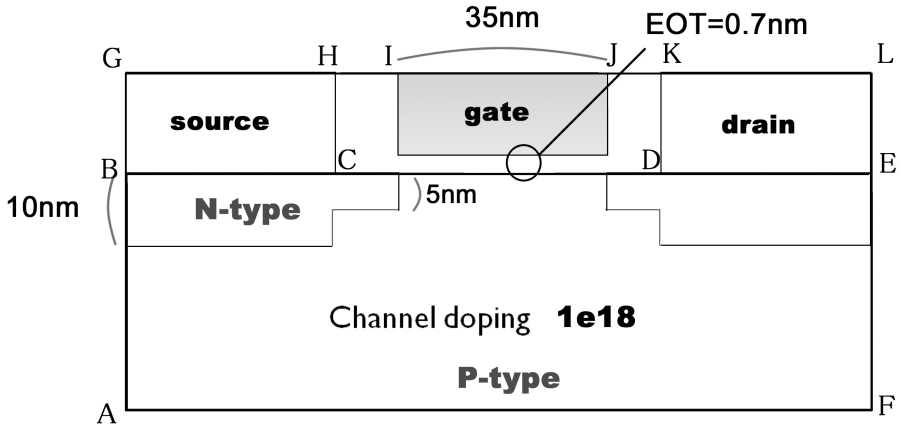

Figure 5.1: Two-dimensional cross section of a 35 nm bulk MOSFET.

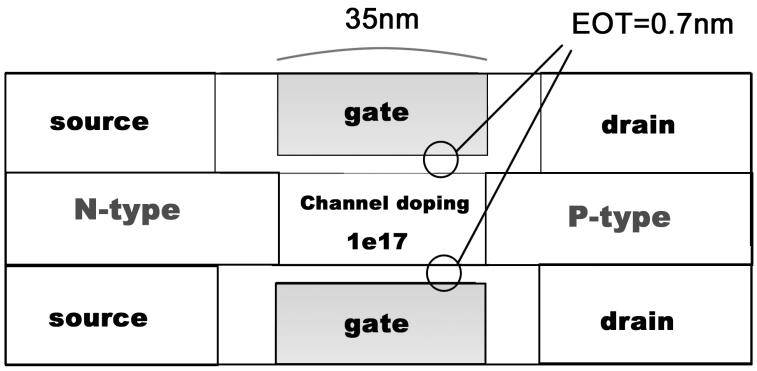

Figure 5.2: Two-dimensional cross section of a 35 nm double gate MOSFET.

5.2 Bulk Si n-MOSFET

In Fig.5.3 (a) and (b), we compare the electron density distributions calculated by QDD, QET and classical ET models. The device was biased with Vg=0.8V and Vd=0.8V. The simulated density distributions are plotted at different positions of the channel. Fig.5.3 (a) shows the electron density distributions perpendicular to the interface at the source end of the channel. The electron density distributions calculated from the QET and QDD models are almost identical in the inversion layers. Carrier heating due to the short channel effects results in the spread of electrons towards the bulk in simulations using the QET and ET models. As a result, the profiles between two models are almost identical at the bulk. The electron density distributions perpendicular to the interface at the drain end of the channel are shown in Fig.5.3 (b). The results clearly indicate that the quantum confinement effect is reduced by the enhanced diffusion towards the bulk due to the high electron temperature near the drain. The QET model allows simulations of quantum confinement transport with hot-carrier effects in MOSFETs.

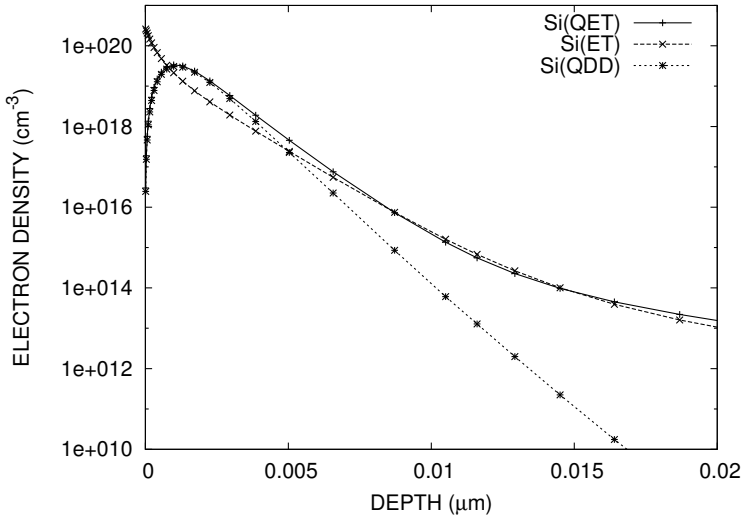

(a)

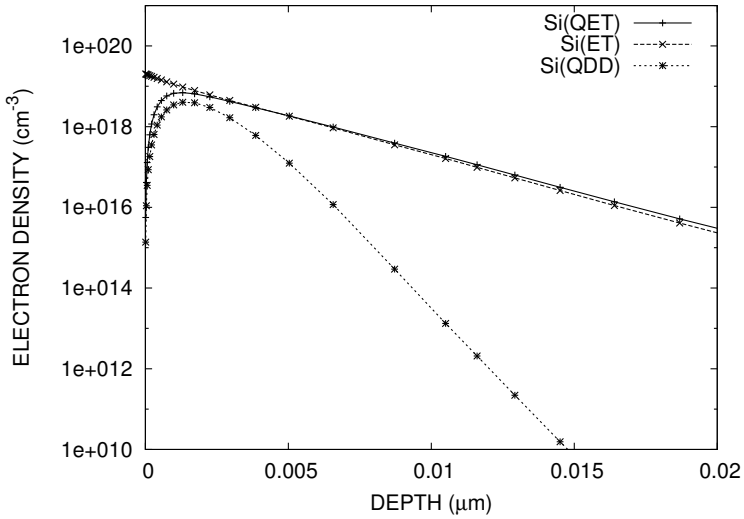

(b)

Figure 5.3: Electron density distributions perpendicular to the interface for a 35nm Si n-MOSFET, (a) at the source end of the channel, (b) at the drain end of the channel. V_g=0.8V, V_d=0.8V.

Fig. 5.4 (a), (b), and (c) shows lateral profiles of electron temperature calculated by the QET and ET models in weak inversion and strong inversion regions, and the medium inversion region between the two. The simulations are done at the same drain voltage of 0.8V. As shown in Fig. 5.4 (a), the results in the weak inversion region are almost identical between two models. In Fig. 5.4 (b), we show the results calculated by the QET model at Vg=0.8V and the ET model at Vg=0.8V and Vg=0.6V. Fig. 5.4 (c) compares the results in the strong inversion region. At the same gate voltage, the QET model exhibits sharper distributions of electron temperature at the lateral direction, when compared to those calculated by the ET model. These differences are caused by the threshold voltage shift due to the quantum confinement in the channel. In Fig. 5.5, we present the x-component of the current density. The results show that the magnitude of the current density calculated by the QET model at Vg=0.8V corresponds to that calculated by the ET model at Vg=0.6V in the medium inversion region. Therefore, the shape of electron temperature distributions is close to that obtained by the ET model at Vg=0.6V, as shown in Fig. 5.4 (b). We can see from Fig. 5.4 (c) a larger discrepancy of temperature distributions in the strong inversion region due to the strong quantum confinement.

Fig.5.6 shows lateral profiles of electron temperature calculated by the QET, QCET, and ET models at the same gate voltage of 1.2V, respectively The simulations are done at the same drain voltage of 0.8V. The quantum corrected ET(QCET) model is a simplified QET model based on Chen's model [13] with a temperature dependent mobility model (2.2.13). In the QCET model, the quantum correction to the energy density is neglected, and the carrier temperature in the current density is approximated by the lattice temperature. As shown in Fig.5.6, the QET model exhibits a sharper temperature distribution of electron temperature at the lateral direction, when compared to that calculated by the classical ET model due to the threshold voltage shift. The electron temperature calculated by the QCET model is further increased.

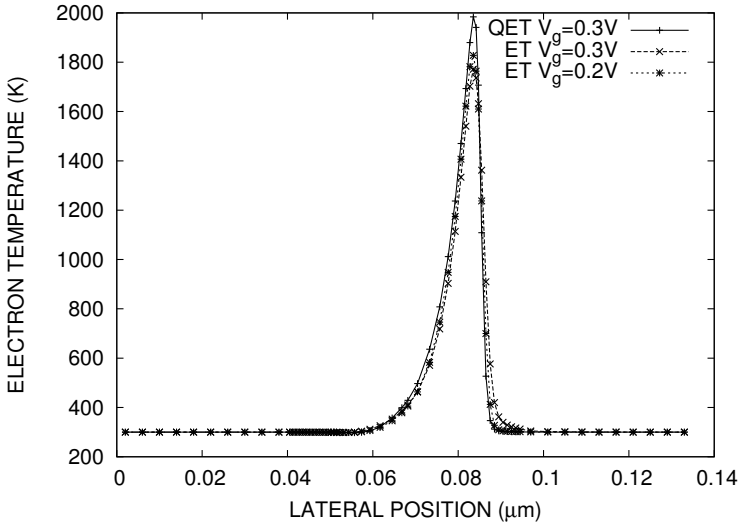
QET V_g=0.3V
ET V_g=0.3V
ET V_g=0.2V
ELECTRON TEMPERATURE (K)
LATERAL POSITION (μm)
2000
1800
1600
1400
1200
1000
800
600
400
200
0
0.02
0.04
0.06
0.08
0.1
0.12
0.14

(a)

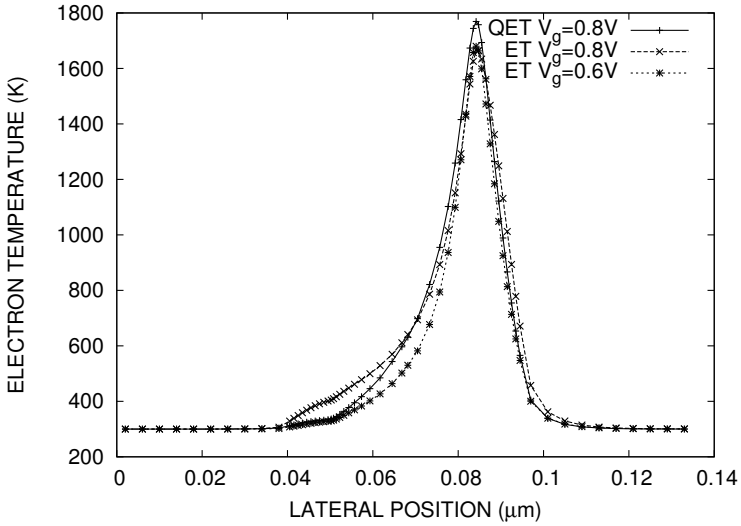
QET V_g=0.8V
ET V_g=0.8V
ET V_g=0.6V
ELECTRON TEMPERATURE (K)
LATERAL POSITION (μm)
1800
1600
1400
1200
1000
800
600
400
200
0
0.02
0.04
0.06
0.08
0.1
0.12
0.14

(b)

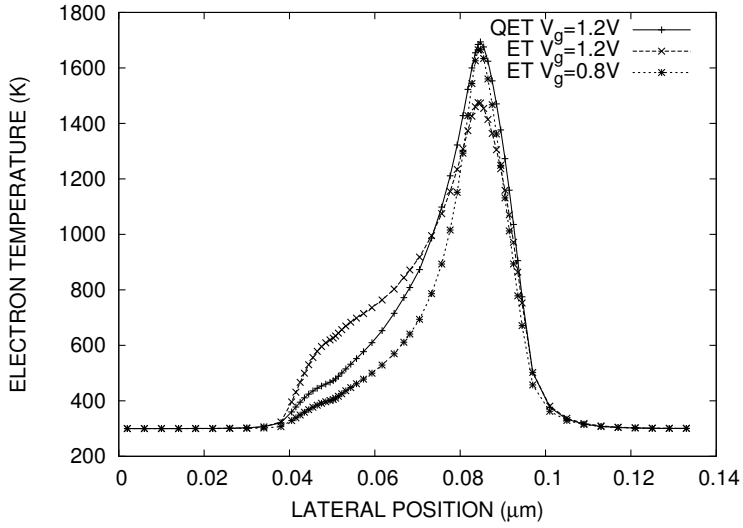

(c)

Figure 5.4: Lateral profiles of electron temperature distributions calculated by QET(solid line) and ET(dotted line) models at the same drain bias of V_d=0.8V. (a) QET model at 0.3V, ET model at V_g=0.3V and V_g=0.2V. (b) QET model at V_g=0.8V, ET model at V_g=0.8V and V_g=0.5V. (c) QET model at 1.2V, ET model at V_g=1.2V and V_g=0.6V.

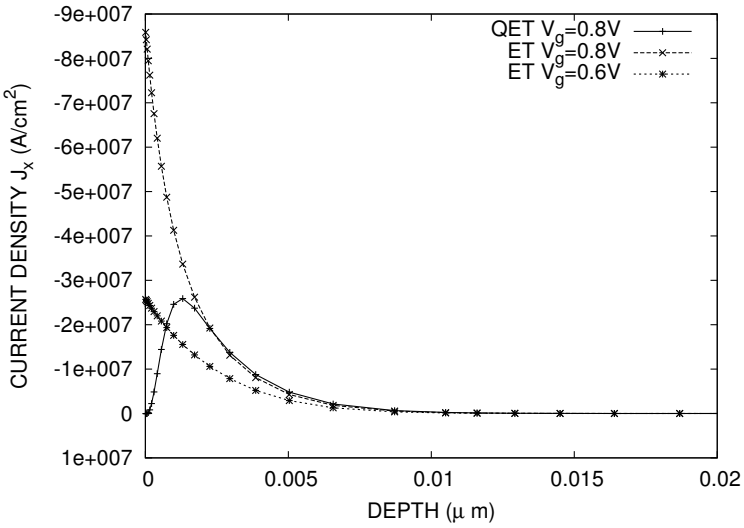

Figure 5.5: x-Component of current densities perpendicular to the interface for a 35nm MOSFET. QET model at Vg=0.8V, ET model at Vg=0.8V and Vg=0.5V

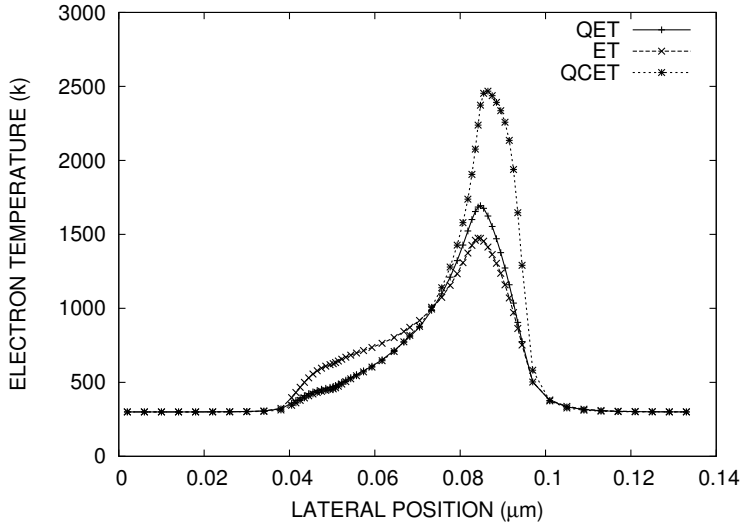

Figure 5.6: Lateral profiles of electron temperature distributions calculated by QET, ET, and QCET models at the same drain bias of V_d=0.8V and the same gate bias of V_g=1.2V.

5.3 Ge and $In_{0.53}Ga_{0.47}As$ n-MOSFETs

Fig. 5.7 (a) and (b) shows comparisons of average inversion layer depths versus effective normal field for Si, Ge, and $In_{0.53}Ga_{0.47}As$ n-MOSFETs. The average inversion layer depth derived in [40] is given as

$$Z_{inv} = \frac{\int_{z_b}^{z_s} z n_{inv} dz}{\int_{z_b}^{z_s} n_{inv} dz}, \tag{5.3.1}$$

where z_b is the bulk (the neutral region under the depletion region) and z_s is the surface. Effective normal field was defined by Sabnis and Clemens [41], which is given by

$$E_{eff} = \frac{1}{\epsilon}(|Q_d| + \eta|Q_i|), \tag{5.3.2}$$

$$Q_d = -q \int_{z_b}^{z_s} (p - C) dz, \tag{5.3.3}$$

$$Q_i = -q \int_{z_b}^{z_s} n dz, \tag{5.3.4}$$

where $\eta = 1/2$ when the carrier is electrons, and $\eta = 1/3$ when the carrier is holes.

Fig. 5.7 (a) shows the comparison of the classical and quantum mechanical av-

erage inversion layer depth for Si, Ge, and $In_{0.53}Ga_{0.47}As$ n-MOSFETs. In all devices, the classical value is less than 1.3 nm, and the difference among three devices is small. Because of the low effective mass and high permittivity of Ge and $In_{0.53}Ga_{0.47}As$, the quantum mechanical value of the Ge n-MOSFET is larger than that of the Si n-MOSFET by 0.8nm-1.0nm. The value is spread to 1.5nm-1.6nm in $In_{0.53}Ga_{0.47}As$ n-MOSFET. This effectively reduces the charge control by the gate in Ge and $In_{0.53}Ga_{0.47}As$ n-MOSFETs. Fig. 5.7 (b) shows average inversion layer depth for two impurity concentrations 1.0×10^{18} cm^{-3} and 1.0×10^{17} cm^{-3}. Although average inversion layer depths have impurity concentration dependence, differences between Si and Ge n-MOSFETs are about 0.8nm-1.0nm for each impurity concentration.

Fig. 5.8 (a) and (b) shows the electron density distributions perpendicular to the interface at the source end and drain end of the channel. The results are calculated by QET and QDD models for Si, Ge, and $In_{0.53}Ga_{0.47}As$ n-MOSFETs. The devices were biased with V_g=0.8V and V_d=0.8V. Similar to the profiles for Si n-MOSFET, the electron density distributions calculated by the QET and QDD models for Ge and $In_{0.53}Ga_{0.47}As$ n-MOSFETs are almost identical at the source end of the channel. The quantum confinement effect is reduced by the enhanced diffusion towards the bulk due to the high electron temperature near the drain. Because of the difference of average inversion layer depth, the quantum confinement effect is further reduced in Ge and $In_{0.53}Ga_{0.47}As$ n-MOSFETs.

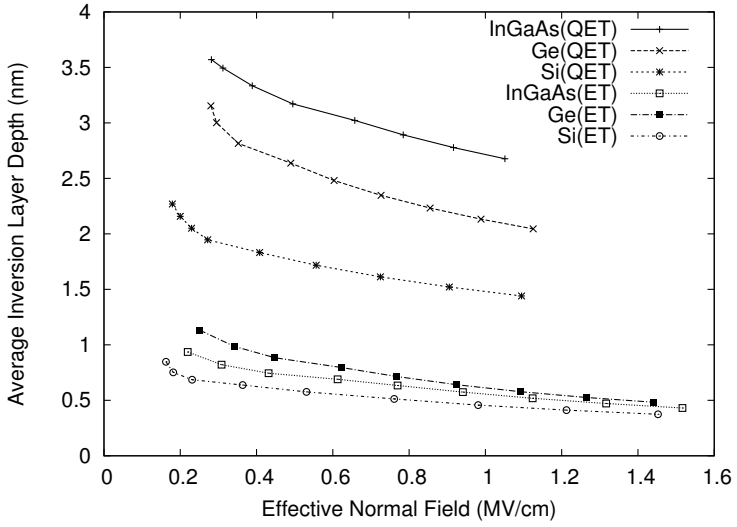

(a)

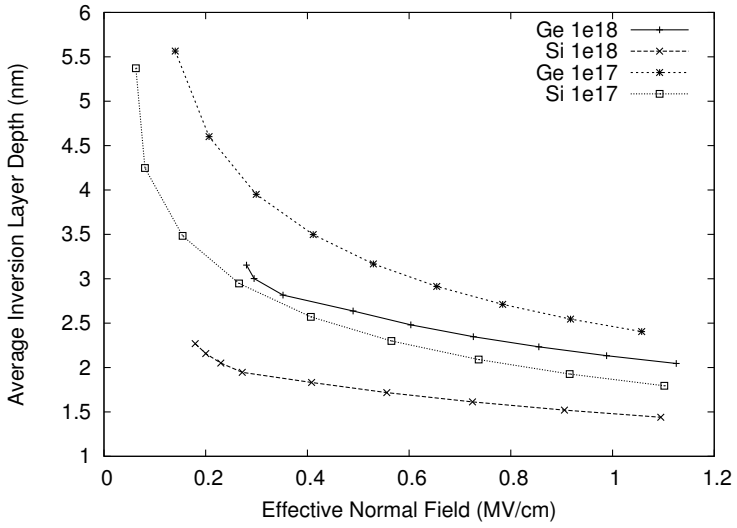

(b)

Figure 5.7: Average inversion layer depth as a function of gate effective normal field for Si and Ge n-MOSFETs. (a) The results are calculated by the QET and ET models. The channel doping is 1.0×10^{18}cm^{-3}. (b) The uniform channel dopings are 1.0×10^{18} cm^{-3} and 1.0×10^{17} cm^{-3}, respectively.

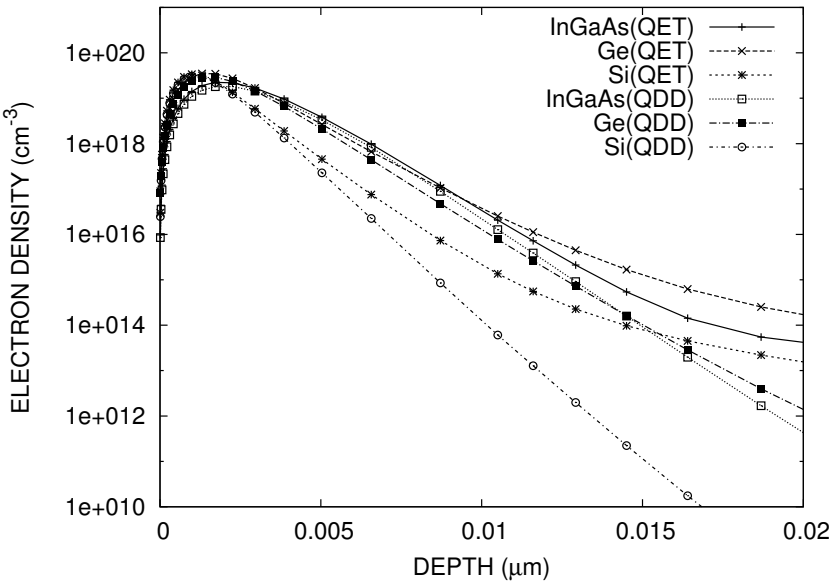

(a)

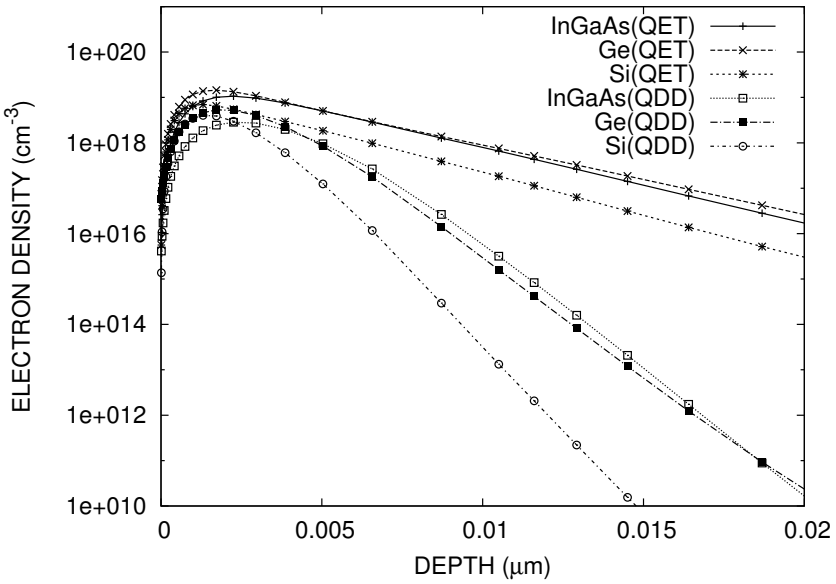

(b)

Figure 5.8: Electron density distributions perpendicular to the interface for a 35nm Si, Ge, and $In_{0.53}Ga_{0.47}As$ n-MOSFETs, (a) at the source end of the channel, (b) at the drain end of the channel. V_g=0.8V, V_d=0.8V.

Fig. 5.9 (a), (b), and (c) shows the electron density distributions at the drain and source ends of the channel for a 35nm Si, Ge, and $In_{0.53}Ga_{0.47}As$ double gate n-MOSFETs. The devices were biased with V_g=0.8V and V_d=0.8V. Fig. 5.9 (a) shows the results of Si double gate n-MOSFET. The silicon layer thickness is 6nm. It is seen that the device exhibits two channels at the source end of the channel and a single channel at the drain end of the channel due to high electron temperature near the drain. Fig. 5.9 (b) and (c) shows the results of Ge and $In_{0.53}Ga_{0.47}As$ double gate n-MOSFETs. Because of the effective degradation of the charge control by the gate, the devices exhibits two channels at the source end of the channel and a single channel at the drain end of the channel at the Ge layer thickness of 8nm and $In_{0.53}Ga_{0.47}As$ layer thickness of 10nm.

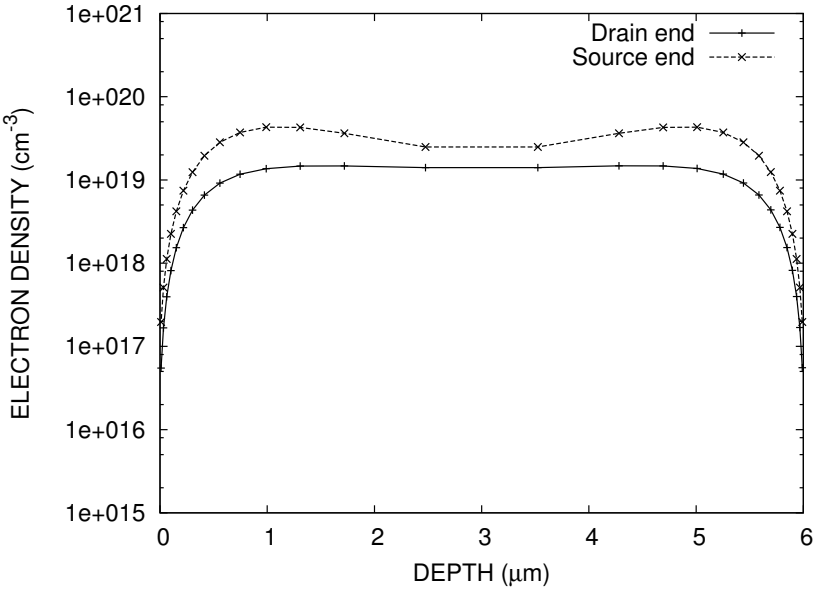
Drain end
Source end
ELECTRON DENSITY (cm-3)
1e+021
1e+020
1e+019
1e+018
1e+017
1e+016
1e+015
0
1
2
3
4
5
6
DEPTH (μm)

(a)

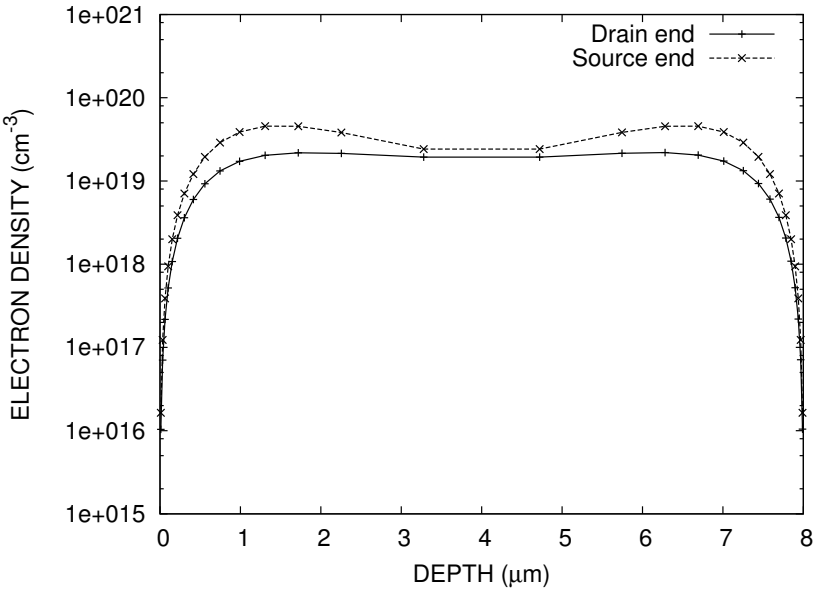
Drain end
Source end
ELECTRON DENSITY (cm-3)
1e+021
1e+020
1e+019
1e+018
1e+017
1e+016
1e+015
0
1
2
3
4
5
6
7
8
DEPTH (μm)

(b)

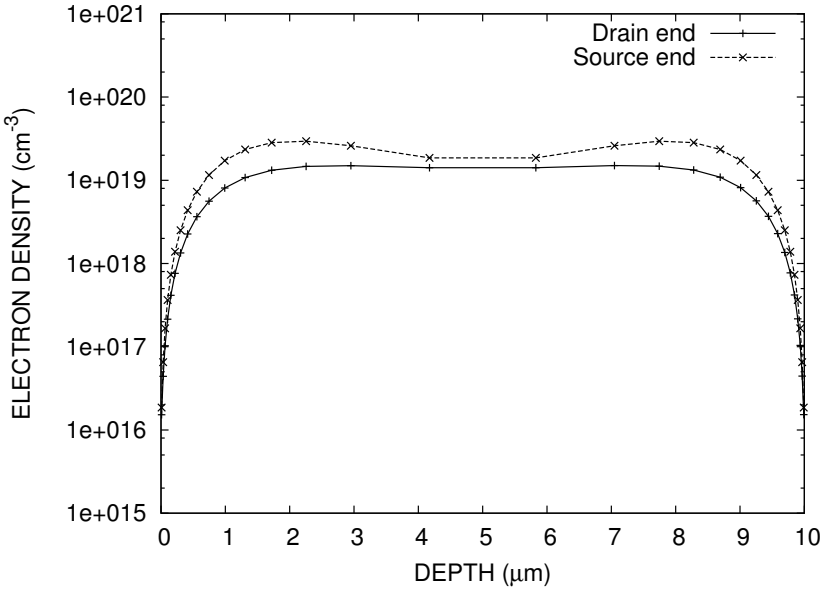

(c)

Figure 5.9: Electron density distributions at the drain and source ends of the channel for a 35nm double gate n-MOSFETs. (a) The results of Si. (b) The results of Ge. (c) The results of $In_{0.53}Ga_{0.47}As$. V_g=0.8V, V_d=0.8V.

Chapter 6

Conclusion

A quantum energy transport(QET) model is obtained by a diffusion approximation in the quantum hydrodynamic equations. We have developed a 4 moments QET model from four moments equations derived from the collisional Wigner-Boltzmann equation to overcome the difficulties associated with the Fourier law closure. The quantum corrections to the energy density and stress tensor are included in the drift contributions to the energy flux density and neglected in the diffusive contributions.

Space discretization of the 4 moments QET model has been performed by a new set of unknown variables. Considering the conservation of the current density and the total energy flow, we construct the same self-adjoint form of the current density J_n and energy flux density S_n, which results in the numerical flux of the finite volume method. Numerical schemes result in a consistent generalization of the Scharfetter-Gummel type scheme to the QET equations. An under relaxation method enhances the robustness of the iterative solution method of the QET system.

Transport properties in Si, Ge and $In_{0.53}Ga_{0.47}As$ n-MOSFETs are evaluated using the 4 moments QET model. The simulation results for bulk and double gate Si, Ge, $In_{0.53}Ga_{0.47}As$ n-MOSFET with high-k/metal gate are obtained. The 4-moments QET model allows simulations of quantum confinement transport with hot-carrier effects in Si, Ge, and $In_{0.53}Ga_{0.47}As$ n-MOSFETs. The simulation results reveal the difference of electron temperature distributions between the QET and classical ET models due to the quantum confinement effects. The charge control by the gate is effectively reduced in the Ge and $In_{0.53}Ga_{0.47}As$ n-MOSFETs due to low effective mass and high permittivity.

The quantum confinement effect is further reduced by high electron temperature near the drain. Double gate n-MOSFETs exhibit two channels at the source end of the channel and a single channel at the drain end of the channel, at the different body thicknesses among Si, Ge, $In_{0.53}Ga_{0.47}As$ n-MOSFETs.

Bibliography

[1] M. Bohr, The evolution of scaling from the homogeneous era to the heterogeneous era, Proc. IEDM (2011), pp. 1-6.

[2] C. L. Gardner, The quantum hydrodynamic model for semiconductor devices, SIAM J. Appl. Math., vol. 24 (1994), pp. 409-427.

[3] A. Jüngel, Transport equations for semiconductors, Lect. Notes Phys. 773, Springer (2009).

[4] K. Bløtekjær, Transport equations for electrons in two-valley semiconductors, IEEE Trans. Electron Devices, vol. ED-17 (1970), pp. 38-47.

[5] T. Grasser, T-W Tang, H. Kosina, and S. Selberherr, A review of hydrodynamic and energy-transport models for semiconductor device simulation, IEEE Proceedings, vol. 91 (2003), pp. 251-274.

[6] J. W. Jerome, Analysis of charge transport: a mathematical study of semiconductor devices, Springer-Verlag (1996).

[7] S-C Lee and T-W Tang, Transport coefficients for a silicon hydrodynamic model extracted from inhomogeneous monte-carlo calculations, Solid-State Elec., vol. 35 (1992), pp. 561-569.

[8] A. Bringer and G. Schön, Extended moment equations for electron transport in semiconducting submicron structures, J. Appl. Phys., vol. 64 (1988), pp. 2447-2455.

[9] R. Thoma, A. Emunds, B. Meinerzhagen, H.J.Peifer, and W.L.Engl, Hydrodynamic equations for semiconductors with nonparabolic band structure, IEEE Trans. Electron Devices, vol. 38 (1991), pp. 1343-1353.

[10] P. Degond, F. Méhats, and C. Ringhofer, Quantum energy transport and drift diffusion models, J. Stat. Phys., vol. 118 (2005), pp. 625-667.

[11] G. Allaire, A. Arnold, P. Degond, and T. Y. Hou, Quantum transport, Springer (2008), pp. 144-152.

[12] S. Jin, Y-J Park, and H-S Min, Simulation of quantum effects in the nano-scale simiconductor device, J. Semi.Tech. and Sci., vol. 4 (2004), pp. 32-38.

[13] R-C Chen and J-L Liu, An accelerated monotone iterative method for the quantum-corrected energy transport model, J. Comp. Phys., vol. 204 (2005), pp. 131-156.

[14] S. Sho and S. Odanaka, A quantum energy transport model for semiconductor device simulation, J. Comp. Phys., 235 (2013), pp. 486-496.

[15] T-W Tang, Extension of the Scharfetter-Gummel algorithm to the energy balance equation, IEEE Trans. Electron Devices, vol. ED-31 (1984), pp. 1912-1914.

[16] M. Rudan and F. Odeh, Multi-dimensional discretization scheme for the hydrodynamic model of semiconductor devices, COMPEL, vol. 5 (1986), no. 3, pp. 149-183.

[17] S. Takagi et al., MOS interface and channel engineering for high-mobility Ge/Ⅲ I-V CMOS, Proc. IEDM (2012), pp. 23.1.1-23.1.4.

[18] A. Rahman et al., Assessment of Ge n-MOSFETs by quantum simulation, Proc. IEDM (2003), pp. 471-474.

[19] M. V. Fischetti and T. P. O 'Regan, Theoretical study of some physical aspects of electronic transport in nMOSFETs at the 10-nm gate-length, IEEE Trans. Electron Devices, vol. 54 (2007), pp. 2116-2136.

[20] S. E. Laux, A simulation study of the switching times of 22- and 17-nm gate-length SOI nFETs on high mobility substrates and Si, IEEE Trans. Electron Devices, vol. 54 (2007), pp. 2304-2320.

[21] R. Quey et al., A temperature dependent model for the saturation velocity in semiconductor materials, Mater. Sci. Semi. Processing, vol. 3 (2000), pp. 149-155.

[22] T. P. O 'Regan et al., Calculation of the electron mobility in Ⅲ-V inversion layers with high-k dielectrics, J. Appl. Phys., vol. 108 (2010), pp. 103705-1-103705-11.

[23] C. Carmody et al., Ion-implanted In0.53Ga0.47As for ultrafast optoelectronic applications, Appl. Phys. Letters, vol. 82 (2003), pp. 3913-3915.

[24] S. Sho, S. Odanaka, and A. Hiroki, Analysis of carrier transport in Si and Ge MOSFETs including quantum confinement and hot carrier effects, Proc. IWCE (2013), pp. 160-161.

[25] S. Sho and S. Odanaka, Advanced MOSFET simulations using a quantum energy transport model, Proc. Society for Silicon Device Material (2013), pp. 32-37. (in Japanese)

[26] M. G. Ancona, and G. J. Iafrate, Quantum correction to the equation of state of an electron gas in a semiconductor, Phys. Rev. B 39 (1989), pp. 9536-9540.

[27] E. Wigner, On the quantum correction for thermodynamic equailibrium, Phys. Rev. 40 (1932), pp. 749-759.

[28] C. S. Rafferty, B. Biegel, Z. Yu, M. G. Ancona, J. Bude, and R. W. Dutton, Multi-dimensional quantum effect simulation using a density-gradient model and script-level programming techniques, Proc. SISPAD (1998), pp. 137-140.

[29] A. Jüngel and R. Pinnau, A positivity-preserving numerical scheme for a nonlinear fourth order parabolic system, SIAM J. Numer. Anal. (2001), pp. 385-406.

[30] M. G. Ancona and H. F. Tiersten, Macroscopic physics of the silicon inversion layer, Phys. Rev. B, 35 (1987), pp. 7959-7965.

[31] M. Gritsch, H. Kosina, T. Grasser, and S. Selberherr, Revision of the standard hydrodynamic transport model for SOI simulation, IEEE Trans. Electron Devices, vol. 49 (2002), pp. 1814-1820.

[32] W. Hänsch and M. Miura-Mattausch, The hot - electron problem in small semiconductor devices, J. Appl. Phys., vol. 60 (1986), pp. 650-656.

[33] S. Odanaka, Multidimensional discretization of the stationary quantum drift-diffusion model for ultrasmall MOSFET structures, IEEE Trans. CAD of ICAS, vol. 23 (2004), pp. 837-842.

[34] A. Forghieri, R. Guerrieri, P. Ciampolini, A. Gnudi, M. Rudan, and G. Baccarani, A new discretization strategy of the semiconductor equations comprising momentum and energy balance, IEEE Trans. CAD, vol. 7 (1988), pp. 231-242.

[35] D. Chen, E-C Kan, U. Ravaioli, C-W, Shu, and R-W Dutton, An improved energy transport model including nonparabolicity and non-Maxwellian distribution effects, IEEE Electron Device Letter, vol. 13 (1992), pp. 26-28.

[36] B. Meinerzhangen and W-L Engl, The influence of the thermal equilibrium approximation on the accuracy of classical two-dimensional numerical modeling of silicon submicrometer MOS transistors, IEEE Trans. Electron Devices, vol. 35 (1988), pp. 689-697.

[37] H. K. Gummel, A self-consistent iterative scheme for one-dimensional steady state transistor calculations, IEEE Trans. Electron Devices, 11 (1964), pp. 455-465.

[38] C. de Falco, E. Gatti, A. L. Lacaita, and R. Sacco, Quantum-corrected drift-diffusion models for transport in semiconductor devices, J. Comp. Phys. vol. 204 (2005), pp. 533-561.

[39] C. de Falco, J. W. Jerome, and R. Sacco, Quantum-corrected drift-diffusion models: Solution fixed point map and finite element approximation, J. Comp. Phys., vol. 228 (2009), pp. 1770-1789.

[40] Y. Ohkura, Quantum effects in Si n-MOS inversion layer at high substrate concentration, Solid-State Elec., vol. 33 (1990), pp. 1581-1585.

[41] A. G. Sabnis and J. T. Clemens. Characterization of the electron mobility in the inverted $\langle 100 \rangle$ Si surface, IEDM (1979), pp. 18-21.

[42] B. L. Anderson and R. L. Anderson, Fundamentals of semiconductor devices, McGraw-Hill (2005).